Medical Image Analysis 35 (2017) 669–684

Contents lists available at ScienceDirect

Medical Image Analysis

journal homepage: www.elsevier.com/locate/media

A framework for combining a motion atlas with non-motion information to learn clinically useful biomarkers: Application to cardiac resynchronisation therapy response prediction

Devis Peressutti[a], Matthew Sinclair[a], Wenjia Bai[b], Thomas Jackson[a], Jacobus Ruijsink[a], David Nordsletten[a], Liya Asner[a], Myrianthi Hadjicharalambous[a], Christopher A. Rinaldi[a], Daniel Rueckert[b], Andrew P. King[a,*]

[a] Division of Imaging Sciences and Biomedical Engineering, King's College London, London, United Kingdom
[b] Biomedical Image Analysis Group, Imperial College London, London, United Kingdom

ARTICLE INFO

Article history:
Received 28 November 2015
Revised 4 October 2016
Accepted 6 October 2016
Available online 11 October 2016

Keywords:
Spatio-temporal atlas
Multiple kernel learning
Random projections
Cardiac resynchronisation therapy

ABSTRACT

We present a framework for combining a cardiac motion atlas with non-motion data. The atlas represents cardiac cycle motion across a number of subjects in a common space based on rich motion descriptors capturing 3D displacement, velocity, strain and strain rate. The non-motion data are derived from a variety of sources such as imaging, electrocardiogram (ECG) and clinical reports. Once in the atlas space, we apply a novel supervised learning approach based on random projections and ensemble learning to learn the relationship between the atlas data and some desired clinical output. We apply our framework to the problem of predicting response to Cardiac Resynchronisation Therapy (CRT). Using a cohort of 34 patients selected for CRT using conventional criteria, results show that the combination of motion and non-motion data enables CRT response to be predicted with 91.2% accuracy (100% sensitivity and 62.5% specificity), which compares favourably with the current state-of-the-art in CRT response prediction.

1. Introduction

The use of spatio-temporal atlases for the statistical analysis of normal and pathological cardiac motion has gained increasing interest over the past decade. The intuition behind such approaches is that pathological changes in the heart lead to altered electromechanical behaviour, and therefore observing the mechanics of cardiac motion may lead to the uncovering of clinically useful information about the pathology. Motivated by this, machine learning based approaches have been proposed that try to identify characteristic motion 'signatures' that are linked to some desired clinical information, such as the presence of specific motion abnormalities in the left ventricle (LV) (Duchateau et al., 2012b).

At the same time, research in the clinical literature has been advancing, and more is now known about the mechanisms underlying heart failure. In addition, a wide range of data is available in clinical records, some of which are likely to be useful in forming biomarkers for different clinical problems. Some of these data are image-derived. For example, in Cardiac Resynchronisation Therapy (CRT), a number of echocardiography-based indices have been proposed for patient selection (Chung et al., 2008), although results have yet to prove conclusive. Other data are derived from the results of simple clinical tests which are often available in the clinical record, such as the six minute walk test (Enright, 2003).

Therefore, there is a wealth of potential information, both motion and non-motion based, that could be used to assist clinicians in making decisions about, for example, patient selection or treatment planning. However, to date, a methodological framework for combining and utilising such disparate sources of information has been lacking. In this paper, we propose such a framework, which facilitates the combined analysis of motion information from a spatio-temporal atlas with non-motion data derived from a variety of sources such as imaging, the electrocardiogram (ECG) or clinical reports. The framework we propose is based on the use of a spatio-temporal atlas for the normalisation of the motion information, followed by multiple kernel learning (MKL) for the combination of motion and non-motion features. We demonstrate its application to the problem of patient selection for CRT, although the framework could be applicable to the analysis of other cardiac conditions. In the following sections we first review the literature on CRT and CRT patient selection, then review relevant work from the

* Corresponding author.
E-mail addresses: devis.1.peressutti@kcl.ac.uk (D. Peressutti), andrew.king@kcl.ac.uk (A.P. King).

http://dx.doi.org/10.1016/j.media.2016.10.002

field of spatio-temporal atlases and MKL, and finally we summarise our novel contributions in this context.

1.1. Cardiac resynchronisation therapy

Pathological impairment of the LV electrical conduction system typically leads to a dyssynchronous electro-mechanical activation that degrades the LV systolic performance, ultimately causing heart failure (HF) (Kirk and Kass, 2013). In the past two decades, CRT has been increasingly employed for the treatment of selected HF patients with electrical dyssynchrony. CRT aims to restore mechanical synchrony by electrically pacing the heart in a synchronised manner (Owen et al., 2009). Standard selection criteria for CRT are a New York Heart Association functional class of II to IV, a QRS duration $\geq$120 ms, and a LV ejection fraction (EF) $\leq$35% (Owen et al., 2009). However, when applying such criteria, approximately 30% and 44% of eligible patients do not show, respectively, clinical (i.e. whether the patient feels better) and volumetric (i.e. whether the LV manifests reverse remodelling) response to the treatment (Abraham et al., 2002; Bleeker et al., 2006; Kirk and Kass, 2013; Daubert et al., 2012). Improvement of the selection criteria for a better characterisation of CRT responders is therefore of great clinical interest.

Recent findings have shown that multiple independent factors correlate with treatment outcome. For instance, Bilchick et al. (2014) have shown that the presence/location of LV myocardial scar and the configuration of pacing leads can influence CRT volumetric response. A strict left bundle branch block (LBBB) (Tian et al., 2013), a type II electrical activation pattern (also known as U-shaped activation) (Sohal et al., 2013; Jackson et al., 2014) and an early activation of the septum (septal flash) (Parsai et al., 2009) have also been shown to correlate with an enhanced level of LV reverse remodelling following CRT. Several studies have also investigated the use of image-derived indices of dyssynchrony for a more accurate characterisation of CRT responders (Santaularia-Tomas and Abraham, 2009). However, to date, no single index has been shown to greatly improve the reliability of CRT patient selection, as reported in the multi-centre PROSPECT study (Chung et al., 2008). Therefore, as highlighted in Jackson et al. (2014) and Parsai et al. (2009), factors such as scar, strict LBBB and septal flash, represent some of the multiple mechanisms that influence CRT response, but may not be good predictors if considered separately.

1.2. Cardiac spatio-temporal atlases

The term *spatio-temporal atlas* (or *motion atlas*) refers to the establishment of a common coordinate system in which population comparisons of motion can be carried out. The use of such atlases for the statistical analysis of normal and pathological LV motion has gained increasing interest over the past decade, showing promising results for patient stratification and for the characterisation of cardiac diseases. Following advances in mathematical tools for the parallel transport of vector fields and tensors (Rao et al., 2002, 2004; Qiu et al., 2009; Lorenzi et al., 2011), statistical spatio-temporal atlases of the LV have been derived from cardiac Magnetic Resonance (CMR) sequences (Chandrashekara et al., 2003; Rougon et al., 2004; Perperidis et al., 2005; Ardekani et al., 2009; Lu et al., 2009; Garcia-Barnes et al., 2010; De Craene et al., 2012; Medrano-Gracia et al., 2013, 2014; Bai et al., 2015), as well as from 2D echocardiography (Duchateau et al., 2011, 2012b) and Computed Tomography (CT) (Hoogendoorn et al., 2013).

Although conceptually similar, these works differ in the techniques used to estimate the LV geometry and motion, to represent the motion, and also their intended application. For instance, Medrano-Gracia et al. (2013) fitted a finite-element model to cine-CMR sequences to estimate the LV motion, and subsequently analysed the shape and motion configuration of the model to detect and quantify infarcted myocardium. With the same application, Suinesiaputra et al. (2009) employed Independent Component Analysis on the distribution of endo- and epi-cardial LV contours derived from cine-MR. These works focussed on the statistical analysis of shapes, without explicitly estimating and transporting motion fields.

A polyaffine motion model has been recently proposed for statistical analysis of LV motion in McLeod et al. (2015a,b). In this approach, the motion of the myocardium is represented as an affine transformation for each of the 17 American Heart Association (AHA) segments, and inter-subject comparisons of these transformations is facilitated by conversion to a prolate spheroidal coordinate system.

More closely related to the proposed framework is the work of Duchateau et al. (2011, 2012b) and De Craene et al. (2012), in which statistical inference on myocardial velocities was proposed to detect septal flash and LV motion abnormalities as compared to the LV motion of healthy subjects. However, in Duchateau et al. (2011, 2012b) the velocities of the LV myocardium were estimated from 2D echocardiography, therefore providing a limited description of the complex 3D mechanical contraction. De Craene et al. (2012) employed tag-CMR sequences to quantify 3D+t myocardial motion abnormalities, but the method was evaluated on only two patients. In Duchateau et al. (2011), the spatio-temporal atlas of the LV septum proposed previously in Duchateau et al. (2010) was employed to assess the changes induced by CRT on the motion of the septum. By using the velocity maps, the authors demonstrated that a correction of the septal flash due to CRT correlated with an enhanced volumetric response.

In the cardiac spatio-temporal atlas works reviewed in this section, a number of motion representations have been employed, including intensity-based (Lu et al., 2009), displacement-based (Chandrashekara et al., 2003; Perperidis et al., 2005; Garcia-Barnes et al., 2010; Bai et al., 2015), velocity-based (Duchateau et al., 2011, 2012b), momentum-based (Ardekani et al., 2009) and polyaffine (McLeod et al., 2015a,b). In Garcia-Barnes et al. (2010) a representation based on 2D strain was employed but the technique performed inter-subject comparisons in a normalised parametric domain and therefore was not a spatio-temporal atlas in the sense discussed here.

1.3. Multiple kernel learning

As well as motion and shape information, several works have attempted to combine such high dimensional data with lower dimensional data from other sources for learning tasks. An early example of this principle is the work by Costa and Hero (2005), in which class labels were used to constrain embeddings computed using non-linear dimensionality reduction. This idea was extended and applied to a medical application in Wolz et al. (2012), who used clinical meta-data to constrain a manifold learnt from MR imaging data for the purpose of Alzheimer's disease stratification.

MKL works on a similar principle to these techniques. MKL algorithms extend Support Vector Machine (SVM) methods by considering a linear or non-linear combination of multiple kernels, as opposed to the single kernel representation of SVM. In particular, MKL offers an optimal solution for the combination of information derived from different sources or modalities, addressing issues related to differences in representation, variability and dimensionality. In MKL, each kernel provides a different measure of similarity between observations, therefore enriching the description necessary to accurately perform the classification/regression task at hand.

MKL methods have been successfully employed in several applications, ranging from genetics, computer vision and medical

imaging. For instance, Hinrichs et al. (2009) have employed MKL to combine features from different image modalities for a more accurate classification of mild Alzheimer's disease subjects. Similarly, Filipovych et al. (2011) used MKL to integrate clinical and imaging data for the prediction of cognitive decline in elderly subjects. More recently, Sanchez-Martinez et al. (2015) have proposed the use of unsupervised MKL to combine cardiac velocity information from different cardiac phases for the identification of heart failure patients with preserved ejection fraction. In this work, we propose the use of MKL to combine non-motion data (see Section 3.2.1) with the motion and deformation information embedded in a spatio-temporal atlas (see Section 3.2.2). The proposed framework is evaluated on a binary classification, although it could be easily extended to a multi-class classification or regression setting.

1.4. Our contributions

The main novelties of the proposed framework are threefold. First, we extend the 3D+t spatio-temporal atlas proposed by Perperidis et al. (2005) and De Craene et al. (2012) to transform not just the localised LV displacements and velocities of different patients to the atlas coordinate system, but also the strains. This enables direct inter-subject comparison of a rich representation of cardiac motion and its properties for each LV location and cardiac phase. Secondly, we employ MKL to combine the motion information provided by the spatio-temporal motion atlas with the non-motion data derived from different sources (e.g. the ECG signal, 2D echocardiography, clinical reports). In this way, a comprehensive description of the electro-mechanical LV activation is provided to more accurately identify CRT volumetric responders and non-responders. To the authors' knowledge, no previous work has exploited the combination of atlas-based high-dimensional motion data and non-motion data for the prediction of CRT response. Thirdly, we adapt the Random Projection ensemble learning method we proposed in Peressutti et al. (2015) for the extraction of the motion features used in the MKL framework.

The paper is structured as follows. Materials used to evaluate the proposed framework are described in Section 2, while the methods are presented in Section 3. A thorough evaluation of the spatio-temporal atlas construction and CRT responders classification is provided in Section 4. Results are presented in Section 5, while a discussion of the results and conclusions are reported in Section 6.

2. Materials

A cohort of 34 patients fulfilling the conventional criteria for CRT (see Section 1.1) was used in this study. The study was approved by the institutional ethics committee and all patients gave written informed consent[1]. All patients underwent CMR prior to CRT and 2D echocardiography imaging and clinical evaluation prior to CRT and at 6-months follow-up.

2.1. CMR imaging

The following CMR sequences were acquired using a 1.5T scanner (Achieva, Philips Healthcare, Best, Netherlands) with a 32-element cardiac coil:

cine-CMR: a multi-slice short-axis (SA) and three single-slice long-axis (LA) (2, 3 and 4-chamber view) 2D cine Steady State Free Precession (SSFP) sequences were acquired (TR/TE = 3.0/1.5 ms, flip angle = 60°). Typical slice thickness is 8 mm for SA and 10 mm for LA with an in-plane resolution $\approx 1.4 \times 1.4$ mm^2;

T-CMR: 3D tagged CMR sequences in three orthogonal directions were acquired (TR/TE = 7.0/3.2 ms, flip angle = 19 – 25°, tag distance = 7 mm, slice thickness = 7 mm). The images have reduced field-of-view enclosing the LV, with typical spatial resolution in the plane orthogonal to the tagging direction $\approx 1.0 \times 1.0$ mm^2;

DE-CMR: delayed-enhancement CMR images were acquired 15–20 min following the administration of 0.1–0.2 mmol/kg gadopentate dimeglumine (Magnevist, Bayer Healthcare, Dublin, Ireland) using conventional inversion recovery sequences. A multi-slice SA and three single-slice LA 2D images were acquired (TR/TE = 5.6/2.0 ms, flip angle = 25°). The same field-of-view and orientation as the cine-CMR sequences was used. The slice thickness of both SA and LA images is 10 mm with an in-plane resolution $\approx 1.4 \times 1.4$ mm^2.

All images were ECG-gated and acquired during sequential breath-holds. Due to the high in-plane spatial resolution, the cine-CMR images at end-diastole (ED) were employed to estimate LV geometry (see Section 3.1), while the remaining cine-CMR images were not used. An average high resolution $3D+t$ T-CMR sequence was derived from the three T-CMR acquisitions with orthogonal tagging directions. The averaged T-CMR sequence was used to estimate the LV contraction (see Section 3.1). The DE-CMR images were used to quantify the extent of LV myocardial scar for use as part of the non-motion data in our framework.

Similar to Shi et al. (2012), prior to the estimation of LV geometry and motion, the SA and LA cine-CMR sequences were spatially aligned to the T-CMR coordinate system. Such spatial alignment compensates for motion occurring between sequential breath-holds. The T-CMR sequence is free from respiratory artefacts and was therefore chosen as the reference coordinate system.

2.2. Non-motion data

The non-motion data employed in this work were derived from the clinical assessment of the patient (*Aetiology*, *Gender*, New York Heart Association class *NYHA*, score of the Quality of Life assessment *QOL*, six minutes walking distance 6*MWD*), from the ECG signal (presence of Left Bundle Branch-Block *LBBB*, duration of the QRS complex QRS_d, QRS complex category QRS_{cat}, *Rhythm*), from the 2D echocardiography imaging acquired prior to CRT (End-Diastolic Volume, End-Systolic Volume and Ejection Fraction (*EDV*, *ESV* and *EF*)) and from the DE-CMR images (*Scar*). Details of the non-motion data are reported in Table 1 and Fig. 1.

Regarding the source of dyssynchrony, 32 out of 34 patients showed electrical dyssynchrony ($QRS_d > 120$ ms), and 21 out of 34 patients showed mechanical dyssynchrony as indicated by an early activation of the septum (septal flash). Patients with strict LBBB were characterised by a longer QRS duration ($\geq$140 ms in men and $\geq$130 ms in women) and a mid-QRS notching (Tian et al., 2013). 13 out of 34 patients had an ischaemic aetiology, although scar was evaluated also for the non-ischaemic patients. For each patient, the LV scar distribution was estimated from the DE-MR images using the cmr^{42} software (Circle Cardiovascular Imaging Inc.). The software requires the observer to delineate the endo- and epi-cardial LV contours and to set an intensity threshold to best separate scarred from healthy myocardium. Two clinical experts independently carried out the quantification of scar distribution. Fig. 1(b) shows an example of a resulting scar map, where the regional enhanced area is specified on a 16 AHA segment model (see Fig. 1(a)). Note that the scar maps produced by the cmr^{42} software do not include segment 17 which represents the apex. The regional enhanced area represented the percentage of scarred

[1] Data were acquired from different projects and cannot be made publicly available due to lack of ethical approval for data sharing.

Table 1
Description of the non-motion data derived from the clinical evaluation of the patient, from the ECG analysis and from 2D echocardiography imaging. For continuous data values, the third column reports mean and standard deviation over the entire cohort, while for categorical (binary) data values, the fourth column reports the counts of the corresponding categories.

Biomarker	Description	Mean/std dev	Frequency
Aetiology	Ischaemic/non-ischaemic	NA	13/21
EDV_m	End-Diastolic Volume from 3D geometry (cm^3)	281/127	NA
EDV	End-Diastolic Volume from 2D echo (cm^3)	214/91	NA
ESV	End-Systolic Volume from 2D echo (cm^3)	164/84	NA
EF	Ejection Fraction from 2D echo (%)	24.7/9.3	NA
Gender	Male/Female	NA	24/10
LBBB	Strict Left-Bundle Branch Block: yes/no	NA	23/11
NYHA	New York Heart Association classes (I-IV)	2.7/0.5	NA
QOL	Quality of Life questionnaire score	48/27	NA
QRS_d	QRS duration (ms)	146/22	NA
QRS_{cat}	QRS category $<$ 150 ms/ $>$ 150 ms	NA	18/16
Rhythm	Sinus/Atrial fibrillation	NA	28/6
6*MWD*	6 min walking distance (m)	269/137	NA

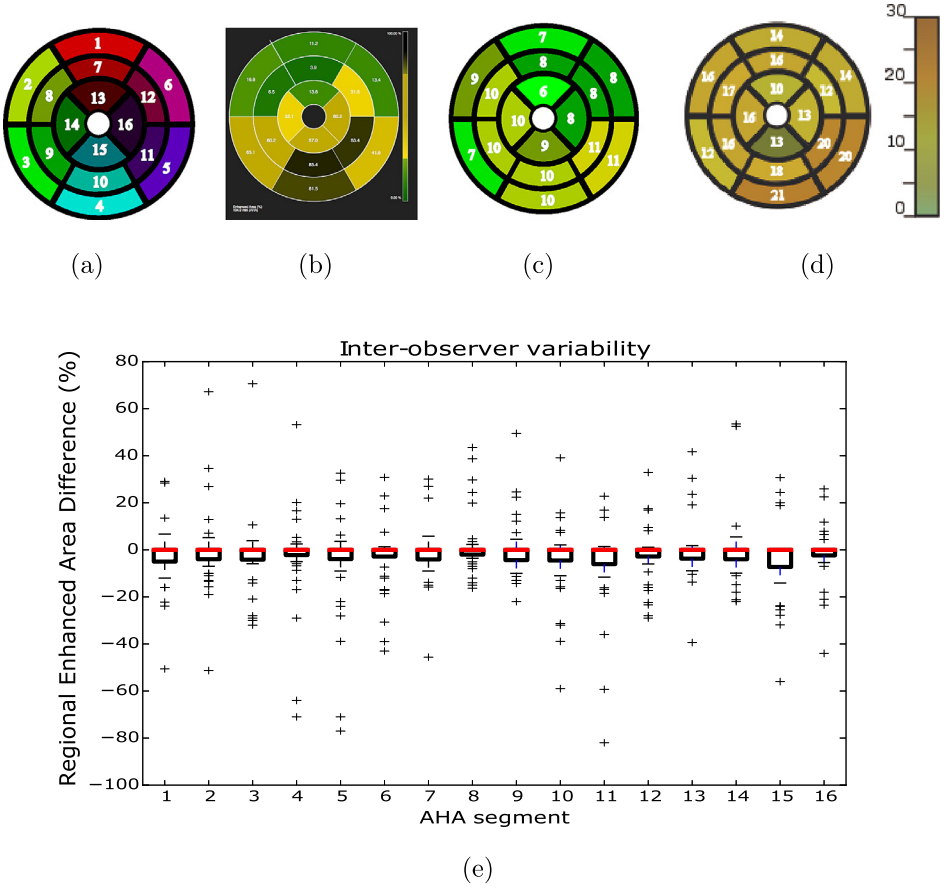

Fig. 1. Non-motion scar data: (a) Colour coded bull's eye plot of the 16 AHA segments. (b) Example of regional enhanced area map returned as output from the cmr42 software. The mean and standard deviation values of regional enhanced area over all patients for each AHA segment are reported in (c) and (d), respectively, with the colour bar indicating the percentage of enhanced area in each segment. The inter-observer variability is illustrated in (e), in which the box plot for each AHA segment shows the difference in enhanced area percentage estimated by observers 1 and 2. Therefore, there are 34 such differences for each segment, one for each patient in our cohort. (For interpretation of the references to colour in this figure legend, the reader is referred to the web version of this article.)

myocardium per AHA segment. The *Scar* data is a 16 valued vector computed as the average value over the two observers for each AHA segment. The mean and standard deviation over all the subjects for each AHA segment are reported in Fig. 1(c) and (d). The inter-observer variability for each AHA segment over all patients is shown in Fig. 1(e).

SA and LA 2D echocardiography imaging was acquired prior to CRT and at 6-months follow-up. Images were acquired using a Philips IE33 ultrasound machine and a X5-1 transducer. The LA views were employed to estimate the *EDV*, *ESV* and *EF*. These values were considered independently and also as a single vector computed as the concatenation of the *EDV*, *ESV* and *EF* values. In addition, the ED volume as computed from the 3D LV medial surface (see Section 3.1.1) was also considered as a complementary descriptor of the LV volume.

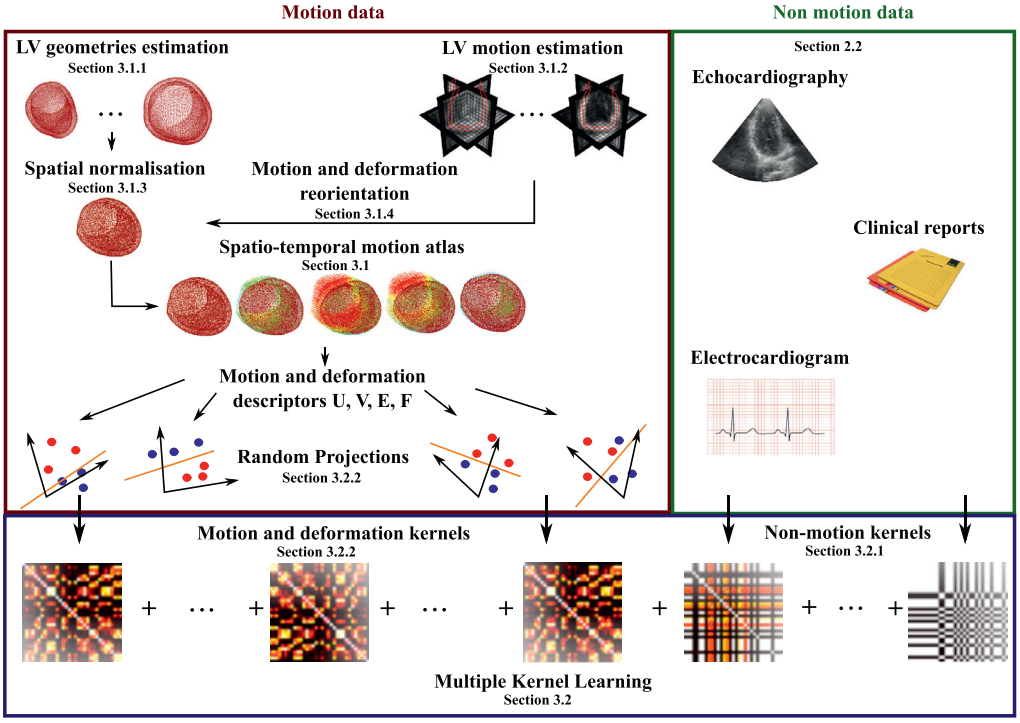

Fig. 2. Overview of the proposed framework to combine motion and non-motion information about the LV function. Motion and deformation of the heart of the population sample is described by a spatio-temporal atlas. Multiple kernel learning combines the information provided by the spatio-temporal atlas with the information provided by non-motion data, such as echocardiography imaging, clinical reports and ECG. This framework can be used for the characterisation of the cardiac function. In this paper, we show its application to the characterisation of CRT responders.

2.3. CRT volumetric response

The classification of CRT response was based on the volumetric measures derived from 2D echocardiography acquired at a 6-months follow-up evaluation. These volumetric measures are commonly employed for the quantification of reverse remodelling (White et al., 1987; Ypenburg et al., 2009). Specifically, the cohort of patients was divided into three non-overlapping classes based on their *ESV* change (i.e. $(ESV_{pre} - ESV_{post})/ESV_{pre}$) as follows:

- **NR:** non-responders, defined as the patients showing an *ESV* change $<15\%$;
- **R:** responders, defined as the patients showing an *ESV* change $\geq 15\%$;
- **SR:** super responders, defined as the patients showing an *EDV* change $\geq 20\%$, an *ESV* change $\geq 15\%$ and a two-fold increase in ejection fraction, or an *EF* absolute value $\geq 40\%$.

As different measures for super-response have been proposed in the literature (António et al., 2009; Tian et al., 2013), the combined measure as described above was employed. Following this classification, our cohort of 34 patients was divided into 8 non-responders, 12 responders and 14 super-responders. This classification was used to train the proposed MKL classifier (see Section 3.2).

3. Methods

The main novelty of the proposed method lies in the combination of atlas-based motion and deformation information with non-motion data derived from several sources such as ECG, clinical reports and echocardiography imaging. An overview of the proposed framework is shown in Fig. 2.

To allow comparison of motion and deformation information across patients, a spatio-temporal motion atlas was built, and motion and deformation features that maximise the classification performance were extracted. Non-motion and motion data were subsequently combined in a MKL framework for a comprehensive description of LV electro-mechanical contraction for an accurate prediction of CRT response.

The construction of the spatio-temporal motion atlas is described in Section 3.1 while the MKL classification is described in Section 3.2.

3.1. Spatio-temporal motion atlas

Similar to De Craene et al. (2012), a spatio-temporal motion atlas of the LV was built to allow motion comparison from different patients. The atlas removes differences in LV shape and cardiac cycle duration from the comparison of LV motion.

The LV spatio-temporal motion atlas formation involves the following steps: estimation of LV geometry and motion, spatial normalisation of LV geometries and motion and deformation reorientation from each subject-specific coordinate system to the atlas coordinate system. Each step is described in the following sections.

3.1.1. Estimation of LV geometry

For each patient, the LV myocardium, excluding papillary muscles, was manually segmented from the ED frames of the multi-slice SA (Fig. 3(a)) and three LA cine CMR images (Fig. 3(b)) and the four binary masks were fused together into an isotropic 2 mm^3 binary image (Fig. 3(c)) by using a binary OR operation. Following further manual smoothing of the binary mask to improve accuracy (Fig. 3(d)), an open-source statistical shape model (SSM) of the LV (Bai et al., 2015) was employed to estimate point correspondence amongst all LV geometries. After an initial rigid alignment based on five landmarks (i.e. endocardial apex, basal anterior and posterior insertion of the right ventricle, basal mid-septum and basal mid-free wall), the SSM was optimised to

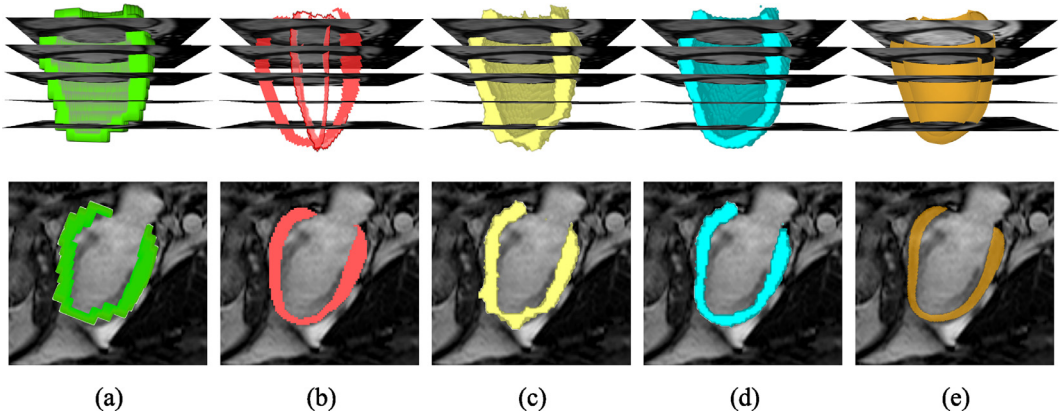

Fig. 3. Illustration of the segmentation and SSM fitting process. A single long-axis image (bottom row) is shown as well as a 3D view with 5 SA image planes and a truncated LV geometry (top row) at each step: (a) LV manual segmentation of the ED SA cine CMR image stack, with a coarse long-axis resolution; (b) LV manual segmentation of the 3 ED LA cine CMR images, with high in-plane resolution (see bottom row), but few projections (see top row); (c) the fused SA and LA mask, with anatomical inaccuracies inherited from (a); (d) the manually smoothed LV segmentation; (e) the optimised SSM fitted to (d).

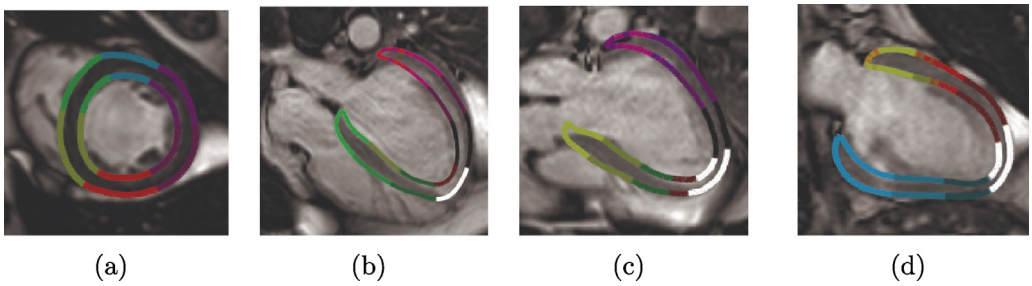

Fig. 4. Example of estimated LV geometry at end-diastole overlaid onto (a) mid SA slice, (b) 4-, (c) 3-, and (d) 2-chamber cine LA slices. Colours encode the 17 AHA regions available from the SSM (see Fig. 1(a) for AHA region correspondence). (For interpretation of the references to colour in this figure legend, the reader is referred to the web version of this article.)

fit the LV binary segmentation. Non-rigid registration followed the mode optimisation to refine local alignment (Fig. 3(e)).

The SSM was derived from a healthy population of 1000+ subjects, and provides a 17 AHA regions segmentation (see Fig. 5). Even though the LV geometries of HF patients significantly differ from healthy LV geometries, the variance captured by the SSM allowed the model to successfully represent pathological geometries. The quality of the segmentation was visually assessed for all patients, as well as the correspondence between the AHA regions of the model and the patient's anatomy. An example of derived LV surfaces is shown in Fig. 4(a) to (d).

In order to spatially reduce and regularise the number of vertices (≈22000) of the SSM surface, a medial surface with regularly sampled vertices (≈3000) was generated from the personalised SSM epi- and endo-cardial surfaces using ray-casting and homogeneous downsampling followed by cell subdivision (Fig. 5). The same resampling strategy was employed for all personalised SSM surfaces to maintain point correspondence. The volume of the derived ED medial surface was also considered as non-motion data as it provides a 3D estimation of LV size, in addition to that derived from 2D echocardiography (see Section 2.2).

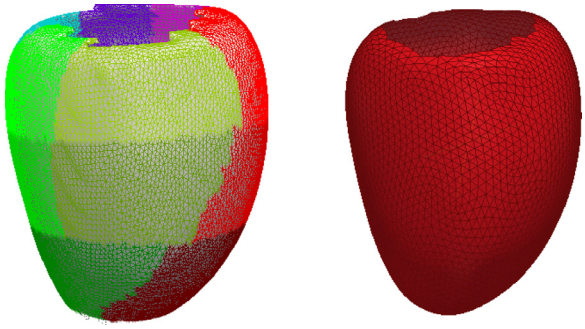

Fig. 5. Example of original SSM with AHA parcellation (left) and corresponding resampled medial surface (right). The aim of the surface resampling was to regularise and reduce the number of vertices of the SSM.

3.1.2. Estimation of LV motion

An average high resolution $3D+t$ T-CMR sequence was derived from the $3D+t$ T-CMR sequences with orthogonal tagging planes. For each T-CMR volume, the trigger time t_T specified in the DICOM meta-tag was normalised with respect to the patient's average cardiac cycle, such that $t_T \in [0, 1)$, with 0 being ED. LV motion and deformation with respect to the ED cardiac phase was estimated using a sequential $3D$ GPU-based free-form deformation (FFD) registration (Rueckert et al., 1999; Chandrashekara et al., 2004). In particular, given the T-CMR image at each cardiac phase, the LV motion was estimated by registering the image with respect to the previous cardiac phase. This way, small deformations between cardiac phases were better estimated and the motion tracking was more robust to the typical intensity fluctuations found in T-CMR images. The sequentially estimated FFD deformation fields were then composed to obtain the FFD transformation from each cardiac phase to the reference ED phase. Furthermore, a $3D+t$ spline interpolation was fitted to the composed 3D transformation in order to estimate a full cycle $3D+t$ transformation, thus achieving temporal normalisation across subjects, regardless of the number of acquired T-CMR volumes and cycle length. The result of the motion estimation was, for each patient n, a smooth $3D+t$ transformation $\psi_n^{3D+t}(\mathbf{x}, t)$

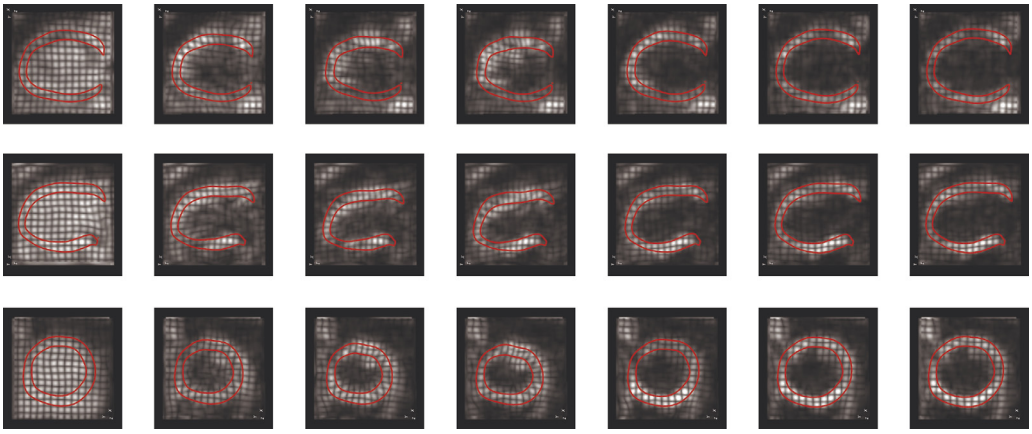

Fig. 6. Example of LV motion estimation. The warped LV endo- and epi-cardial mesh surfaces (red lines) are overlaid onto the corresponding T-CMR images at different cardiac phases (left-to-right), starting from ED (left-most). The top two rows show orthogonal LA mid-cavity slices, and the bottom row shows a mid-cavity SA slice. (For interpretation of the references to colour in this figure legend, the reader is referred to the web version of this article.)

Note that the temporal normalisation employed in our framework differs from the work of Duchateau et al. (2011, 2012b) and De Craene et al. (2012), where specific cardiac events were aligned across subjects. We normalise only with respect to the length of the cardiac cycle and rely on the subsequent learning algorithm to uncover the important characteristics of the remaining temporal variation.

An example of motion tracking is shown in Fig. 6.

3.1.3. Spatial normalisation

The aim of spatial normalisation is to remove bias towards patient-specific LV geometries from the motion and deformation analysis. From the previous steps, LV surfaces at the ED phase were derived for each of the N patients. An initial Procrustes alignment based on the point correspondence was performed on the N medial LV surfaces, obtaining a set of affine transformations $\{\phi_n^{aff}\}, n = 1, \ldots, N$ with respect to a randomly chosen reference. An unbiased LV medial surface was computed by transforming the average of the aligned surfaces by the inverse of the average affine transformation $\tilde{\phi}^{aff} = \frac{1}{n}\sum_n \phi_n^{aff}$.

To enforce an identity average transformation, the original transformations $\{\phi_n^{aff}\}$ were similarly normalised $\hat{\phi}_n^{aff} = \phi_n^{aff} \circ (\tilde{\phi}^{aff})^{-1}$. All surfaces were consequently aligned to the unbiased medial LV surface using Thin Plate Spline (TPS) transformations $\{\phi_n^{TPS}\}$. The transformation from the patient-specific coordinate system to the unbiased LV surface is therefore given by $\phi_n = \phi_n^{TPS} \circ \hat{\phi}_n^{aff}$ (De Craene et al., 2012).

3.1.4. Motion and deformation reorientation

This section describes how motion and deformation were first resampled to ensure temporal correspondence between subjects, and then transported into a common atlas coordinate system to facilitate inter-subject comparison.

In order to compare cardiac phases amongst all patients, for each patient, the reference ED medial surface was warped to $T = 30$ cardiac phases equally distributed in [0, 1) by using the estimated $3D+t$ FFD transformation $\psi_n^{3D+t}(\mathbf{x}, t)$ as follows. Denoting by $\mathbf{x}_{n,p,0} \in \mathcal{R}^3$ the spatial coordinates of the vertex p at the ED cardiac phase $t = 0$ for a given patient n, the spatial coordinates of the vertex at an evenly sampled time t_s is computed as $\mathbf{x}_{n,p,t_s} = \psi_n^{3D+t}(\mathbf{x}_{n,p,0}, t_s)$. Furthermore, the Jacobian matrix $J_{\psi_n^{3D+t}}$ of the transformation ψ_n^{3D+t} was estimated at each vertex p of the reference ED surface, for each time step t_s, $s = 1, .., T$. The estimation of the Jacobian matrix allows the computation of the Green strain tensor (Bonet and Wood, 2008) with respect to the reference (undeformed) state as

$$E_{n,p,t_s} = \frac{1}{2}\left(J^T_{\mathbf{x}_{n,p,t_s}} J_{\mathbf{x}_{n,p,t_s}} - \mathbb{I}\right), \tag{1}$$

where $\mathbb{I}$ represents the identity matrix. Eq. (1) describes the local deformations that the LV myocardium at location $\mathbf{x}_{n,p,0}$ at the reference ED phase undergoes at the cardiac phase t_s. In this study, along with displacement and velocity, strain and strain rate were considered as motion descriptors, since recent studies have shown their correlation with pathological changes of the myocardial tissue (e.g. scarred tissue) (Maret et al., 2009).

As a result of the surface warping, for each patient n, the displacements $\mathbf{u}_{n,p,t_s} = \mathbf{x}_{n,p,t_s} - \mathbf{x}_{n,p,0}$, velocities $\mathbf{v}_{n,p,t_s} = (\mathbf{x}_{n,p,t_s} - \mathbf{x}_{n,p,t_{s-1}})/\Delta t_s$ and Jacobians $J_{\mathbf{x}_{n,p,t_s}} \in \mathcal{R}^{3\times3}$ were computed for all vertices p of the reference ED surface and for any evenly distributed time $t_s \in [0, 1)$, $\Delta t_s = 1/T$.

The next stage was to transport the displacement, velocity and strain data for each subject into the atlas coordinate system. Under a small deformation assumption (Ashburner, 2007), the following two techniques have been proposed for the parallel transport of vector fields:

PFV: push-forward action on velocities (Duchateau et al., 2011; De Craene et al., 2012; Duchateau et al., 2012a)

$$\mathbf{v}^{\text{atlas}}_{n,p,t_s} = J_{\phi_n(\mathbf{x}_{n,p,0})} J^{-1}_{\mathbf{x}_{n,p,t_s}} \mathbf{v}_{n,p,t_s}, \tag{2}$$

$$\mathbf{u}^{\text{atlas}}_{n,p,t_s} = \mathbf{u}^{\text{atlas}}_{n,p,t_{s-1}} + \mathbf{v}^{\text{atlas}}_{n,p,t_s} \Delta t_s, \tag{3}$$

PFD: push-forward action on displacements (Rao et al., 2002, 2004; Perperidis et al., 2005)

$$\mathbf{u}^{\text{atlas}}_{n,p,t_s} = J_{\phi_n(\mathbf{x}_{n,p,0})} \mathbf{u}_{n,p,t_s}, \tag{4}$$

where $J_{\phi_n(\mathbf{x}_{n,p,0})}$ is the Jacobian of the anatomical transformation ϕ_n mapping each patient's reference ED surface to the atlas ED surface computed at location $\mathbf{x}_{n,p,0}$, while $J_{\mathbf{x}_{n,p,t_s}}$ is the Jacobian of the motion transformation $\psi_n^{3D+t}(\mathbf{x}_{n,p,0}, t_s)$ mapping the reference ED surface to each cardiac phase t_s of patient n.

In this paper, both parallel transport methods were used to transport the displacement and velocity fields to the atlas coordinate system, and the difference between the transformed locations was compared. The results of the PFV and PFD comparison are reported in Section 4.1.

In both methods, the location of the vertex $\mathbf{x}^{\text{atlas}}_{n,p,t_s}$ at cardiac phase t_s is computed as the application of the estimated displacement $\mathbf{u}^{\text{atlas}}_{n,p,t_s}$ to the reference ED atlas location $\mathbf{x}^{\text{atlas}}_{n,p,0}$. After

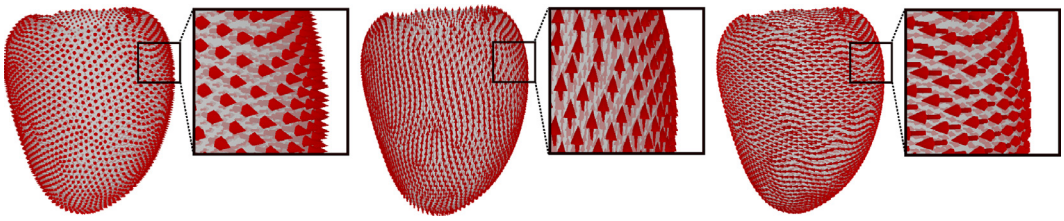

Fig. 7. Example of radial (left), longitudinal (middle) and circumferential (right) directional vectors shown on the medial atlas ED surface.

parallel transport, displacements $\mathbf{u}^{\text{atlas}}_{n,p,t_s} = \mathbf{x}^{\text{atlas}}_{n,p,t_s} - \mathbf{x}^{\text{atlas}}_{n,p,0}$ and velocities $\mathbf{v}^{\text{atlas}}_{n,p,t_s} = (\mathbf{x}^{\text{atlas}}_{n,p,t_s} - \mathbf{x}^{\text{atlas}}_{n,p,t_{s-1}})/\Delta t_s$ can be directly compared across subjects.

In order to allow comparison of strain across subjects, the Jacobians of the $3D+t$ motion transformations $J_{\psi_n^{3D+t}}$ were transformed to the atlas coordinate system as follows:

$$J_{\psi^{\text{atlas}}_{n,3D+t}} = J_{\phi_n} J_{\psi_n^{3D+t}} J^{-1}_{\phi_n}. \tag{5}$$

Eq. (5) corresponds to a change of coordinates of a linear function, where the Jacobians are a linear approximation of a non-linear transformation. Details of the derivation of Eq. (5) are reported in Appendix A. The Jacobian matrices $J_{\psi^{\text{atlas}}_{n,3D+t}}$ and strains $E^{\text{atlas}}_{n,p,t_s}$ (see Eq. (1)) were computed in the atlas coordinate system for each vertex p and cardiac phase t_s.

3.1.5. Local coordinate system

For a more intuitive understanding of the LV motion, displacements, velocities and strains in the atlas coordinate system were projected onto a local cylindrical coordinate system, therefore providing radial, longitudinal, and circumferential information. The long axis of the LV ED atlas surface was used as the longitudinal direction (see Fig. 7). Denoting by **r, l, c** the radial, longitudinal and circumferential unit column vectors, the strain tensor matrices $E^{\text{atlas}}_{n,p,t_s}$ were projected onto the cylindrical coordinate system as

$$\mathcal{E}^{\text{atlas}}_{n,p,t_s} = P^T \cdot E^{\text{atlas}}_{n,p,t_s} \cdot P, \tag{6}$$

where $P = [\mathbf{r}, \mathbf{l}, \mathbf{c}]$. The cylindrical components of strain $\mathbf{e}^{\text{atlas}}_{n,p,t_s} = [e^r_{n,p,t_s}, e^l_{n,p,t_s}, e^c_{n,p,t_s}]$ were computed as the main diagonal of $\mathcal{E}^{\text{atlas}}_{n,p,t_s}$; strain rate was then computed as $\mathbf{f}^{\text{atlas}}_{n,p,t_s} = (\mathbf{e}^{\text{atlas}}_{n,p,t_s} - \mathbf{e}^{\text{atlas}}_{n,p,t_{s-1}})/\Delta t_s$.

3.2. Multiple kernel learning

We now describe the use of a MKL framework to utilise the atlas motion data described in the previous section, as well as the non-motion data outlined in Section 2.2. Recall from Section 1.3 that MKL methods extend SVM methods by considering a linear or non-linear combination of multiple kernels. In a binary classification setting, given a sample of N independent and identically distributed training instances $\{(\mathbf{z}_i, y_i \in \pm 1)\}_{i=1}^N$ where $\mathbf{z}_i$ is the D-dimensional input vector and y_i is its class label, a typical SVM model is given by the linear discriminant function

$$f(\mathbf{z}) = \sum_{i=1}^{N} \alpha_i y_i k(\mathbf{z}_i, \mathbf{z}) + b. \tag{7}$$

In the linear MKL framework, the single kernel function of SVM is replaced by a linear combination of multiple kernel functions $k(\mathbf{z}_i, \mathbf{z}) = \sum_{m=1}^{M} \beta_m k_m(\mathbf{z}_i, \mathbf{z}), \quad \beta_m \geq 0$ such that the linear discriminant function becomes

$$f(\mathbf{z}) = \sum_{i=1}^{N} \alpha_i y_i \sum_{m=1}^{M} \beta_m k_m(\mathbf{z}_i, \mathbf{z}) + b. \tag{8}$$

MKL algorithms seek to optimise both the coefficients $\{\alpha_i\}_{i=1}^N$ and $\{\beta_m\}_{m=1}^M$.

3.2.1. Non-motion kernels

Gaussian Radial Basis Function (RBF) kernels $k_m(\mathbf{z}_i, \mathbf{z}) = \exp(-\frac{\|\mathbf{z}_i - \mathbf{z}\|_2^2}{\sigma_m^2})$ were computed from the non-motion data described in Section 2.2. The bandwidth for each kernel σ_m was estimated from the structure of the data, as proposed in Sanchez-Martinez et al. (2015). In detail, for data with continuous values, the pairwise Euclidean distances were computed over all patients, and the average distance over the closest N/3 neighbours was employed as σ_m. The selected size of the neighbourhood N/3 roughly matched the size of the CRT response classes considered and also approximates the likelihood of volumetric non-responders in a cohort of CRT patients. In the case of binary data $\{\pm 1\}$ (e.g. *Aetiology, Gender*), the bandwidth was fixed to $\sigma_m = 0.1$ to generate binary values of the kernels k_m.

Fig. 8 shows the resulting RBF kernels for the non-motion data considered in this study.

3.2.2. Motion and deformation kernels

Given the high dimensionality of the motion and deformation data, low-dimensional features relevant for the classification of CRT responders were extracted. In this work, the Random Projection ensemble learning approach proposed in Peressutti et al. (2015), which was previously shown to outperform the use of Principal Components Analysis for the classification of CRT super responders, was adapted to the MKL framework as follows.

Following the parallel transport of LV motion and deformation to the atlas coordinate system (see Section 3.1.4), displacement $\mathbf{u}^{\text{atlas}}_{n,p,t_s}$, velocity $\mathbf{v}^{\text{atlas}}_{n,p,t_s}$, strain $\mathbf{e}^{\text{atlas}}_{n,p,t_s}$ and strain rate $\mathbf{f}^{\text{atlas}}_{n,p,t_s}$ vectors in the radial, longitudinal and circumferential directions were available for each patient n, at each vertex p of the atlas surface and for each cardiac phase $t_s \in [0, 1)$. As the T-CMR sequences covered on average $\approx$ 75% of the cardiac cycle (see Fig. 10), only the first $T_s = 22$ out of $T = 30$ evenly sampled cardiac phases were considered for the following analysis, as for $t_s > 0.75$ the estimated motion was due to interpolation only. Furthermore, for each patient n, the vertices of the reference ED medial surface that fell outside of the field-of-view (FoV) of the T-CMR images were removed from the analysis. Most of the removed vertices either belonged to the LV apex or base.

For each patient n, the displacement, velocity, strain and strain rate vectors were concatenated over the remaining P_{FoV} vertices in the FoV and over $t_s \in [0, 0.75)$ to obtain the column vectors $\mathbf{u}^{\text{atlas}}_n \in \mathcal{R}^H$, $\mathbf{v}^{\text{atlas}}_n \in \mathcal{R}^H$, $\mathbf{e}^{\text{atlas}}_n \in \mathcal{R}^H$ and $\mathbf{f}^{\text{atlas}}_n \in \mathcal{R}^H$, where $H = 3P_{FoV}T_s$. The matrices $\mathbf{U} = [\mathbf{u}^{\text{atlas}}_1, .., \mathbf{u}^{\text{atlas}}_N] \in \mathcal{R}^{H\times N}$, $\mathbf{V} = [\mathbf{v}^{\text{atlas}}_1, .., \mathbf{v}^{\text{atlas}}_N] \in \mathcal{R}^{H\times N}$, $\mathbf{E} = [\mathbf{e}^{\text{atlas}}_1, .., \mathbf{e}^{\text{atlas}}_N] \in \mathcal{R}^{H\times N}$, $\mathbf{F} = [\mathbf{f}^{\text{atlas}}_1, .., \mathbf{f}^{\text{atlas}}_N] \in \mathcal{R}^{H\times N}$ were subsequently computed. These matrices represent the LV motion and deformation of the patients in the cohort in the atlas coordinate system.

Given the very high dimensionality H of the motion and deformation matrices, methods for the extraction of meaningful low-dimensional features for the classification of CRT responders need be applied. Random Projections (RPs) have recently gained interest in the fields of pattern recognition and machine learning for

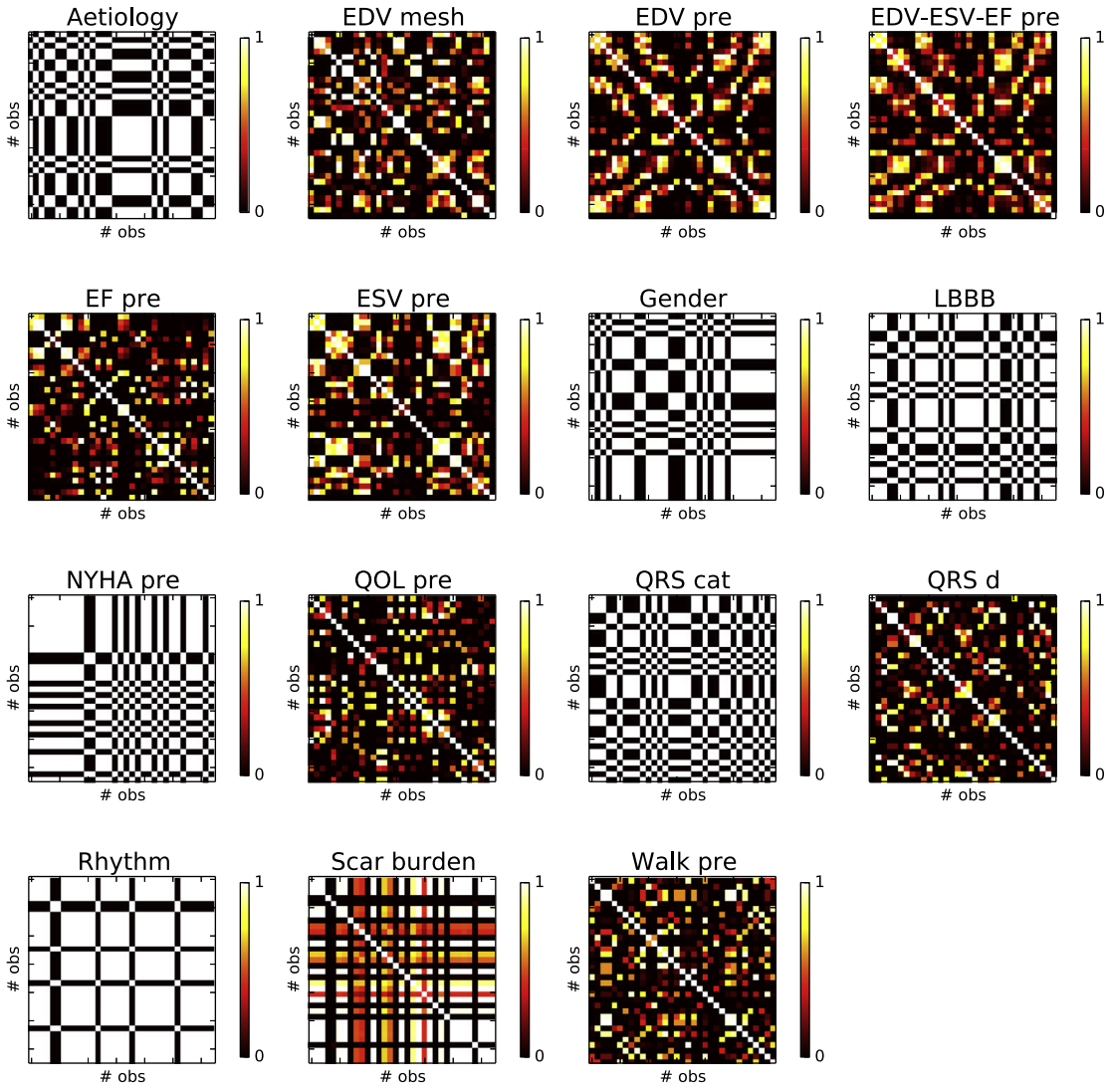

Fig. 8. Example of resulting RBF kernels for non-motion data (see Section 2.2). Each kernel represents the similarity between patients for each non-motion data feature. MKL weights the contributions of each of these kernels to maximise the margin between classes.

dimensionality reduction and feature extraction (Johnson and Lindenstrauss, 1984; Hegde et al., 2008). The underlying concept of RPs is to project the input high dimensional space into a low-dimensional random subspace, where the distance between observations is preserved up to a distortion factor ϵ, which depends on the number of observations and the dimension of the generated subspace (Johnson and Lindenstrauss, 1984). RPs represent a simple and flexible dimensionality reduction method that does not enforce any constraint on the dimensionality reduction of the data, as opposed to other linear (e.g. Principal Component Analysis) or non-linear (e.g. Isomaps, Laplacian Eigenmaps) dimensionality reduction techniques (Yan et al., 2007).

Similar to the Random Projections ensemble learning approach we proposed in Peressutti et al. (2015), an ensemble of L classifiers was created by projecting the input high dimensional matrices **U, V, E** and $\mathbf{F} \in \mathcal{R}^{H\times N}$ onto random low-dimensional subspaces defined by random sparse matrices $\mathbf{R}_l \in \mathcal{R}^{h\times H}$, $h \ll H$, in which the elements of each column vector $\{\mathbf{r}_i\}_{i=1}^{H}$ are drawn from a Bernoulli $\{\pm 1\}$ distribution with $\|\mathbf{r}_i\| = 1$. As a result of the random projections, new low-dimensional motion and deformation descriptors $\mathbf{Z_U} = \mathbf{R}_l\mathbf{U}, \mathbf{Z_V} = \mathbf{R}_l\mathbf{V}, \mathbf{Z_E} = \mathbf{R}_l\mathbf{E}$ and $\mathbf{Z_F} = \mathbf{R}_l\mathbf{F} \in \mathcal{R}^{h\times N}$ were generated. Subsequently, using a 5-fold cross-validation on the training data, an SVM classifier was trained on a Gaussian RBF kernel computed considering the new descriptors $\{\mathbf{z_U}_i\}_{i=1}^{N}$, $\{\mathbf{z_V}_i\}_{i=1}^{N}$, $\{\mathbf{z_E}_i\}_{i=1}^{N}$, $\{\mathbf{z_F}_i\}_{i=1}^{N}$ as input observations. The bandwidth of the RBF kernels was determined considering the Euclidean distance between observations, as detailed in Section 3.2.1. The L random projections generating an accuracy in classification greater than 90% were retained. This process was carried out independently for the displacement, velocity, strain and strain rate matrices, leading to L random projections for each matrix **U, V, E** and **F**. Finally, only three out of the L random projections were randomly selected, resulting in 12 motion-based RBF kernels (i.e. three RPs descriptors and associated RBF kernels each for displacement $\{\mathbf{Z_U}_j\}_{j=1}^{3}$, velocity $\{\mathbf{Z_V}_j\}_{j=1}^{3}$, strain $\{\mathbf{Z_E}_j\}_{j=1}^{3}$ and strain rate $\{\mathbf{Z_F}_j\}_{j=1}^{3}$). The values of h and L are reported in Section 4.

3.2.3. Optimisation

In this work, a total of $M = 27$ kernel functions k_m were employed, 15 derived from non-motion data and 12 derived from motion data. The number of motion kernels was chosen to balance with the number of non-motion kernels, but a larger number of motion kernels could be employed. For the optimisation of the objective function described in Eq. (8), the unknown vectors $\boldsymbol{\alpha}$ and $\boldsymbol{\beta}$ are estimated in a two-step optimisation strategy, with each

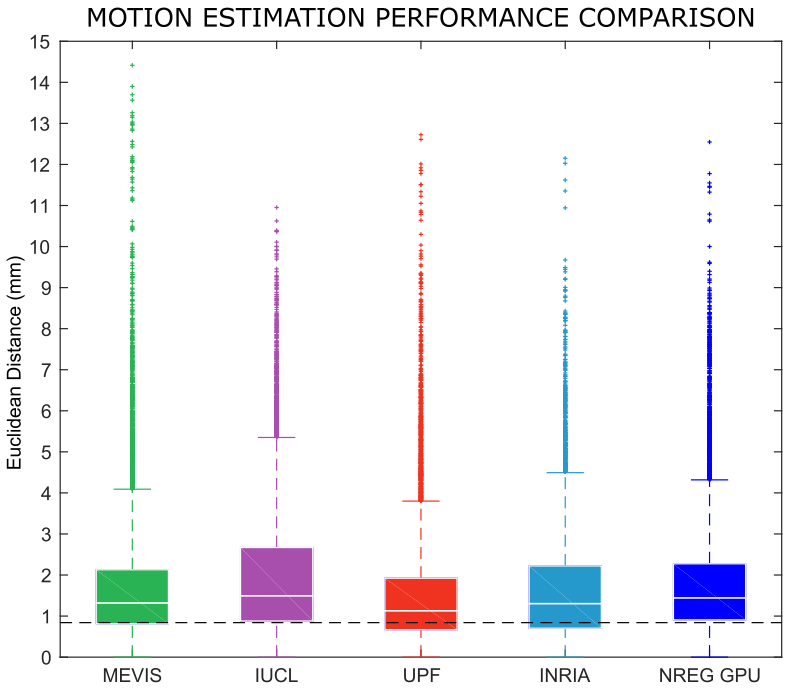

Fig. 9. Motion estimation error. The Euclidean distance between the gold-standard and estimated position of the manually annotated landmarks is reported over all volunteer datasets and cardiac phases, as described in Tobon-Gomez et al. (2013). The GPU-based FFD registration employed in this study (NREG GPU) shows an accuracy performance comparable to state-of-the-art registration methods. The black dashed line represents the inter-observer variability of the manual landmark tracking.

vector being optimised in alternate steps. A l_2-MKL simplex solver was employed , as implemented in the Simple MKL toolbox[2]. This algorithm was chosen for its popularity and open source availability, although different MKL algorithms could have been employed instead. The free parameters of the solver are the misclassification cost value C and the regularisation parameter λ. In particular, C is a positive-defined trade-off parameter between model simplicity and classification error, while λ is the Lagrangian coefficient in the dual Lagrangian formulation of Eq. (8) that acts as a regularisation coefficient (Rakotomamonjy et al., 2008). These parameters were determined through a grid search. Details of the optimal values are reported in the following section.

Note that the MKL optimisation algorithm employed in this study can be seen as an application of the generic framework for dimensionality reduction proposed by Lin et al. (2011).

4. Experiments

Two sets of experiments were performed. The first set of experiments aimed at validating the construction of the spatio-temporal atlas, while the second set of experiments aimed at validating the classification of CRT responders using the proposed MKL framework. Details of the first set of experiments are reported in Section 4.1, while Section 4.2 reports details of the MKL framework validation.

4.1. Spatio-temporal motion atlas

In this set of experiments, the accuracy of the LV segmentation, LV motion estimation and the effect of the parallel transport techniques was evaluated.

In order to estimate the SSM fitting error for LV segmentation, the Dice Similarilty Coefficient (DSC) was computed between the manually refined binary mask (see Fig. 3(d)) and the binary mask derived from the fitted SSM (see Fig. 3(e)). Mean and standard deviation values for the DSC over the 34 datasets were 0.89 ± 0.02, with minimum and maximum DSC of 0.85 and 0.92, respectively. The low value of the standard deviation demonstrates the robustness of the SSM fitting. Fig. 3 shows an example of the SSM fitted to a manually refined binary mask.

Regarding the evaluation of the motion estimation, open-source benchmark T-CMR sequences of the LV from 15 healthy volunteers were employed (Tobon-Gomez et al., 2013). For each T-CMR sequence, manually annotated landmarks were provided as gold-standard and target fiducial errors could be computed. Fig. 9 shows the motion estimation error achieved by the $3D+t$ FFD transformation as compared to state-of-the-art motion tracking methods (Tobon-Gomez et al., 2013). The GPU-based FFD registration achieved tracking accuracy comparable to state-of-the-art methods, allowing the processing of an entire T-CMR sequence in less than 15 min. The $3D+t$ spline fitting error was also computed, showing a mean and mean max error of 0.069 mm and 1.32 mm, respectively.

As detailed in Section 3.1.4, two techniques for the parallel transport of vector fields were compared, namely a push-forward action on velocities (PFV) and a push-forward action on displacements (PFD). In Fig. 10, the displacements transformed to the atlas coordinate system with the two methods are compared. The first row of Fig. 10 shows, for each patient (represented by the different coloured lines), the radial, longitudinal and circumferential components of the mean displacements computed by PFD over all vertices P and for each cardiac phase t_s, while the second row reports the same results for the PFV. The third row shows the resulting difference in mean displacements obtained with the PFD and the PFV. As can be noted in the second and third rows of Fig. 10, the displacements computed by PFV manifest an offset, meaning that the obtained motion is not cyclic. This is due to errors accumulating in the iterative estimation of the displacements (see Eq. (3)). This confirms the findings of Duchateau et al. (2011), where a technique to compensate for the drift was proposed. The absolute difference

[2] http://www.shogun-toolbox.org/doc/en/latest/index.html.

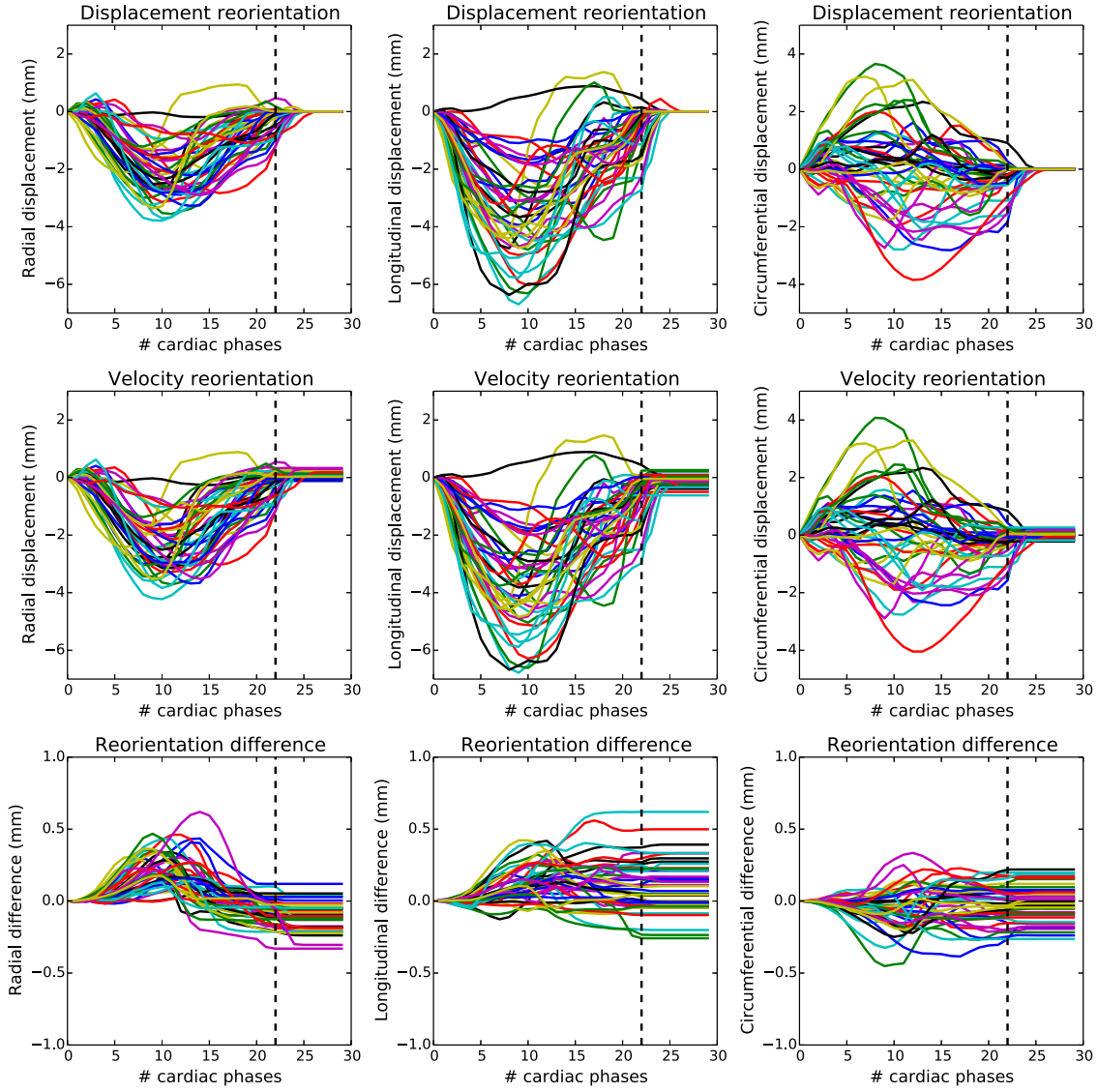

Fig. 10. Comparison of PFV and PFD reorientation. The mean displacements in the atlas coordinate system for each patient n as computed by PFD (first row) and PFV (second row). The first, second and third columns respectively report radial, longitudinal and circumferential components of displacements. The third row shows the difference in displacements between the two reorientation methods. The colours represent the data for the different patients. The PFV reorientation generates an offset in estimation that needs to be compensated for (Duchateau et al., 2011). The black dashed line represents $t_s \approx 0.75$. (For interpretation of the references to colour in this figure legend, the reader is referred to the web version of this article.)

$\|\mathbf{u}_{n,p,t_s}^{atlas,PFD} - \mathbf{u}_{n,p,t_s}^{atlas,PFV}\|$ was computed over all patients n, vertices p and cardiac phases t_s, resulting in median and 75th percentile values of 0.08 mm and 0.16 mm, respectively. Despite the very small difference between the two reorientation techniques, we employed the PFD reorientation for the transport of the motion features used in the MKL framework, as it did not require any drift compensation.

4.2. Multiple kernel learning

This set of experiments aimed at evaluating the classification performance of the proposed MKL framework. Two separate binary classifications were performed. First, the classification of super-responders (SR) against non-responders and responders ($NR + R$) was investigated. In this experiment, the super-responders SR were considered as positive classification samples. Secondly, the classification of non-responders (NR) against responders and super-responders ($R + SR$) was considered. In this classification, the non-responders NR were the negative samples, while $R + SR$ were the positive samples. While the first classification aims at characterising the patients that will benefit most from CRT, the second classification seeks to characterise patients who would not benefit from CRT. The second classification is of particular clinical interest for the improvement of patient selection, as it would avoid unnecessary treatment and costs.

To test the performance of the proposed MKL framework, for both types of classification, the following experiments were carried out:

(i) SVM classification using each non-motion and motion kernel separately;
(ii) MKL classification using non-motion kernels;
(iii) MKL classification using twelve motion kernels (three per motion descriptor) with Random Projections;
(iv) The proposed MKL classification using non-motion and four motion kernels (one per motion descriptor) without Random Projections;

Table 2
Accuracy results for experiment (i), non-motion kernels. The first row reports classification accuracy of super-responders, while the second row reports results for the classification of non-responders. The highest accuracy results are highlighted in bold font.

	Aetiology	EDV_m	EDV	EDV-ESV-EF	EF	ESV	Gender	LBBB	NYHA	QOL	QRS cat	QRS d	Rhythm	Scar	6MWD
NR + R vs SR	58.8	67.6	55.9	61.8	44.1	41.2	44.1	**73.5**	58.8	67.6	**82.4**	64.7	58.8	67.6	35.3
NR vs R + SR	**76.5**	67.6	67.6	61.8	67.6	70.6	**76.5**	**76.5**	**76.5**	70.6	**76.5**	64.7	**76.5**	61.8	55.9

Table 3
Accuracy results for experiment (i), motion kernels. The first row reports classification accuracy of super-responders, while the second row reports results for the classification of non-responders. The highest accuracy results are highlighted in bold font.

	Displ 1	Displ 2	Displ 3	Vel 1	Vel 2	Vel 3	Strain 1	Strain 2	Strain 3	Strain-rate 1	Strain-rate 2	Strain-rate 3
NR + R vs SR	70.6	61.8	55.9	**79.4**	**79.4**	**79.4**	70.6	70.6	70.6	**82.4**	73.5	**79.4**
NR vs R + SR	**79.4**	**76.5**	73.5	67.5	73.5	73.5	67.6	61.8	70.6	73.5	70.6	73.5

(v) The proposed MKL classification using non-motion and four motion kernels (one per motion descriptor) with Random Projections;
(vi) The proposed MKL classification using non-motion and twelve motion kernels (three per motion descriptor) with Random Projections.

A leave-one-out cross-validation was employed for all classifications tested. This means that, in turn, each patient's non-motion and motion descriptors were not considered for the training of the classifier, but used for testing only.

The free parameters of the proposed MKL framework are the dimensions of the random subspace h, the number of random projections L, and the cost C and regularisation λ term in the optimisation of MKL. The dimension of the random subspace h was set to $h = \sqrt{H}$. Given the low number of observations N, this value provided a good trade-off between the introduced distortion $\epsilon < 0.3$ (Johnson and Lindenstrauss, 1984) and the reduction in dimensionality. The number of random projections L providing a training cross-validation accuracy $> 90\%$ was set to $L = 10$. Out of the best L random projections, either one (*v*) or three (*vi*) were randomly chosen for each motion descriptor (see Section 3.2.2). Comparison of experiments (*iv*) and (*v*) allows evaluation of the influence of Random Projections, while comparison of experiment (*v*) and (*vi*) allows evaluation of the optimal number of kernels. For experiments (*ii*)–(*vi*), the optimal values of C and λ were determined through a grid search using all patients in our cohort. This way, we sought to determine and compare the best possible classification results for each experiment.

Classification results for each experiment and corresponding values of C and λ are reported in Section 5.

5. Results

This section reports classification results for the experiments described in Section 4.2.

The accuracy results of the binary classification of super-responders (NR+R vs. SR) and non-responders (NR vs. R+SR) considering each non-motion and motion kernel separately are reported in Tables 2 and 3. Classification accuracy was computed as the sum of true positives and true negatives divided by the number of patients N. Regarding the classification of super-responders, the QRS_{cat} and strict *LBBB* showed good predictive power with an accuracy of 82.4% and 73.5%, in line with the findings reported by Tian et al. (2013) and Jackson et al. (2014). Amongst the motion and deformation kernels, velocity and strain rate data showed the best accuracy values of 79.4% and 82.4%. Concerning the classification of non-responders, the best classification accuracy for non-motion kernels of 76.5% was achieved by the *Aetiology, Gender, LBBB, NYHA* and QRS_{cat}. For motion kernels, displacement showed the best accuracy of 76.5% and 79.4%.

Table 4
Super-responder classification results for MKL using (ii) non-motion kernels, (iii) 12 motion kernels with RPs, (iv) both non-motion and four motion kernels without RPs, (v) both non-motion and four motion kernels with RPs, and (vi) both non-motion and 12 motion kernels with RPs. The highest accuracy results are highlighted in bold font. The number of false positives and false negatives for the proposed technique (*vi*) were respectively 0 and 2.

NR + R vs. SR	(*ii*) %	(*iii*) %	(*iv*) %	(*v*) %	(*vi*) %
Accuracy	**94.1**	91.2	**94.1**	**94.1**	**94.1**
Sensitivity	**85.7**	78.6	**85.7**	**85.7**	**85.7**
Specificity	**100**	100	**100**	**100**	**100**
PPV	**100**	100	**100**	**100**	**100**
NPV	**90.9**	86.9	**90.9**	**90.9**	**90.9**
C	1.2	1.7	1.2	1.2	1.2
λ	2.3	0.5	2.3	2.3	2.3

Table 5
Non-responder classification results for MKL using (ii) non-motion kernels, (iii) 12 motion kernels with RPs, (iv) both non-motion and four motion kernels without RPs, (v) both non-motion and four motion kernels with RPs, and (vi) both non-motion and 12 motion kernels with RPs. The highest accuracy results are highlighted in bold font. The number of false positives and false negatives for the proposed technique (*vi*) were respectively 3 and 0.

NR vs. R + SR	(*ii*) %	(*iii*) %	(*iv*) %	(*v*) %	(*vi*) %
Accuracy	85.3	88.2	88.2	88.2	**91.2**
Sensitivity	100	100	100	100	**100**
Specificity	37.5	50.0	50.0	50.0	**62.5**
PPV	83.8	86.7	86.7	86.7	**89.7**
NPV	100	100	100	100	**100**
C	1.1	1.4	1.2	1.2	0.8
λ	2.2	3.6	2.71	2.7	2.3

The results of experiments (*ii*)–(*vi*) on the classification of super-responders are reported in Table 4, while Table 5 reports results on the classification of non-responders. Compared to experiment (*i*) where non-motion and motion predictors were considered separately, higher classification results were achieved with MKL in both classification of super-responders and non-responders. In the classification of super-responders, the same classification accuracy of 94.1% was achieved by non-motion kernels (*ii*) and all kernels together (*iv*)–(*vi*). In the classification of non-responders, the best accuracy of 91.2% was achieved by the proposed MKL framework (*vi*), in which non-motion and twelve motion kernels were considered together. Motion kernels (*iii*) achieved better classification results compared to non-motion kernels (*ii*), highlighting

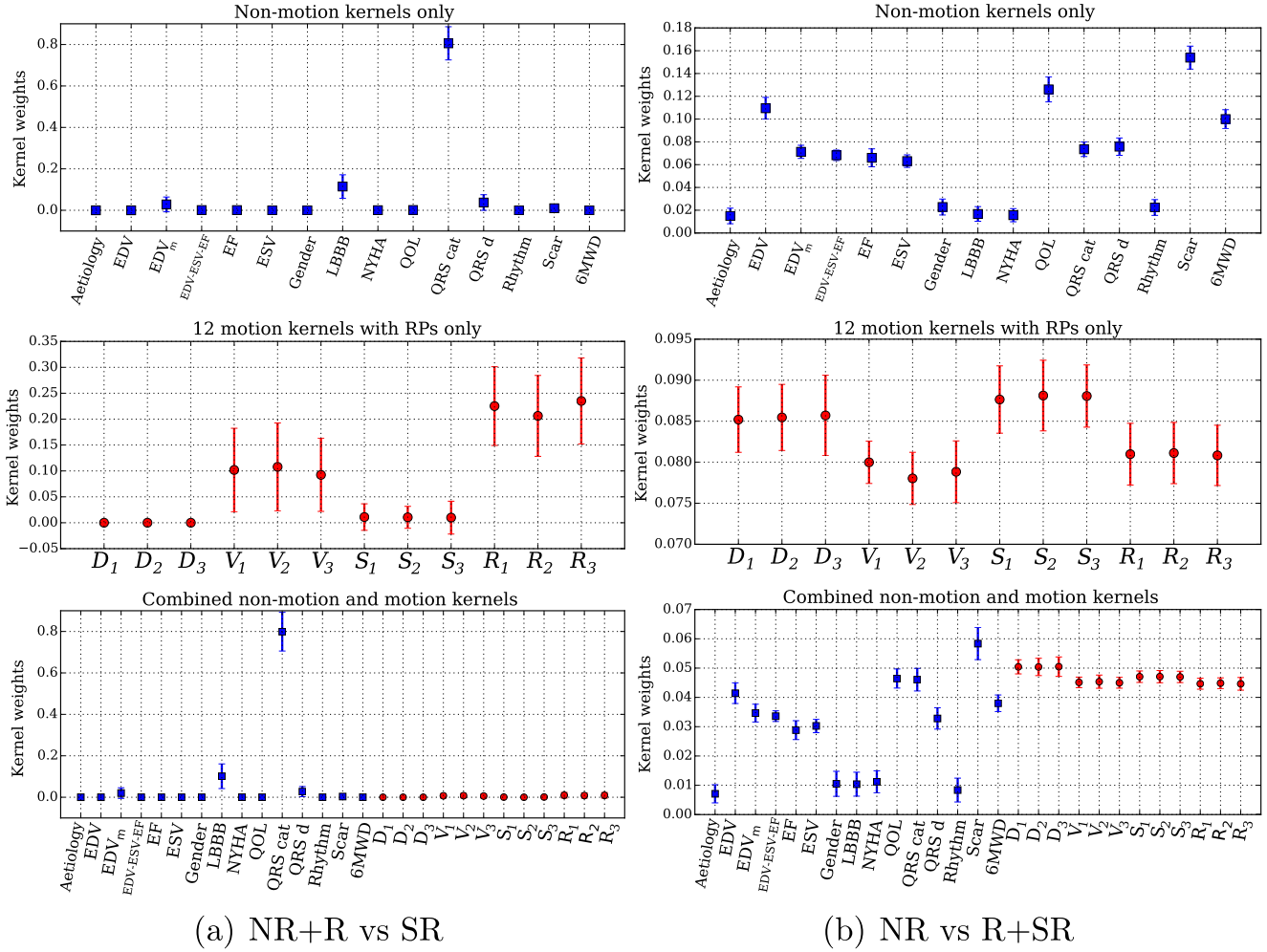

Fig. 11. The mean ± SD of the kernel weights for the leave-one-out cross-validation in experiments (*ii*) non-motion kernels only (top row), (*iii*) 12 motion kernels with RPs only (middle row), in which D, V, S, R represent the displacement, velocity, strain and strain rate kernels respectively, and (*vi*) combined kernels of (*ii*) and (*iii*) (bottom row) for the two classifications (a) NR + R vs SR and (b) NR vs R + SR. For experiment (*vi*), motion kernels have very little weighting relative to a few key non-motion kernels (QRS_{cat}, *LBBB* and QRS_d) in super-responder prediction (bottom row of (a)), but have much more importance in non-responder prediction (the bottom row of (b)).

the importance of motion information in characterising LV electromechanical contraction. Regarding the influence of RPs and the number of kernels, while no difference was found for the classification of super-responders, the best performance in the classification of non-responders was achieved by combining the non-motion descriptors with twelve motion descriptors using RPs. The use of multiple motion kernels per motion descriptor (three each) with RPs provides an improved set of projections for the classification of non-responders, compared to non-motion kernels alone as well as combined non-motion and motion kernels using single motion kernels per descriptor (both with and without RPs).

Fig. 11(a) and (b) shows the mean and standard deviation values of the weights β_m for the leave-one-out validation for experiments (*ii*), (*iii*) and (*vi*) for both classifications. The analysis of these weights provides insight into the influence of the non-motion and motion descriptors in each classification task. In the classification of super-responders, the *LBBB* and QRS_{cat} descriptors mainly drive the classification, while velocity and strain rate contribute most for the motion descriptors. Note that other features that are correlated with these main features (e.g. QRS_d is correlated with QRS_{cat}) have lower weights because, in the presence of the main features, they do not provide extra predictive power to the classification task. Regarding the classification of *NR* vs. $R + SR$, the *Scar*, displacement and strain descriptors contribute most to the classification.

6. Discussion and conclusions

We have proposed a technique for predicting CRT (super) response based on a combination of a cardiac motion atlas with non-motion data obtained from several sources. Spatio-Temporal atlases have previously been proposed for a range of problems. However, until now they have utilised motion data alone (i.e. displacements (Chandrashekara et al., 2003; Perperidis et al., 2005; Garcia-Barnes et al., 2010; Bai et al., 2015) or velocities (Duchateau et al., 2011, 2012b)). In this paper, we have demonstrated a framework for combining such atlases with a range of non-motion data that is often available in clinical reports but which has been rarely exploited in the medical image analysis literature.

Our framework is based on MKL. MKL has been used before in medical imaging, for example for combining clinical with imaging data (Filipovych et al., 2011) and for combining different types of motion feature (Sanchez-Martinez et al., 2015). Our framework uses MKL to combine motion data with non-motion data. To the authors' knowledge, this is the first time that such a technique has been proposed. Furthermore, we utilise a rich description of motion, featuring 3-D displacement, velocity, strain and strain rate in

atlas space for the first time. We also incorporate into the framework our novel supervised learning technique based on random projections and ensemble learning, which we have previously proposed for CRT super response identificaton. (Peressutti et al., 2015).

The results of our technique for prediction of CRT response (i.e. 100%/62.5% sensitivity/specificity) compare well with the current state-of-the-art. For example, Sohal et al. (2014) reported 85% sensitivity and 82% specificity for predicting CRT responders based on volume-change systolic dyssynchrony index. Jackson et al. (2014) reported 78% accuracy (which equated to 76% sensitivity and 100% specificity based on the data they reported), by identifying a type II activation pattern. It is important to give an intuitive interpretation of these figures. The sensitivity figure for CRT response refers to the proportion of potential responders who, if the test were to be used to select patients for treatment, would have been selected. Therefore, 100% minus the sensitivity represents the proportion of responders who would have been denied treatment which would have been successful. Therefore, this is a key figure, since the main aim of a diagnostic test should be to not deny patients treatment that would benefit them. Our technique achieved a sensitivity of 100%, meaning that no potential responders would have been denied treatment. The specificity figure refers to the proportion of non-responders who would be spared the invasive procedure if the test were used. We achieved 62.5%, meaning that almost two thirds of non-responders would be spared the unnecessary treatment.

Looking at our results in more detail, it is apparent that, for CRT super response classification, no improvement was obtained by incorporating motion kernels: the non-motion kernels produced good classification performance (85.7% sensitivity, 100% specificity) on their own. This is likely because CRT super response is known to be associated with specific electromechanical phenomena such as a strict LBBB (Tian et al., 2013), which can be identified by some non-motion data. The more general class of CRT responders represent a more heterogeneous population, with potentially a number of different underlying mechanisms involved. This is reflected in the fact that, for classifying CRT response (i.e. the realistic clinical scenario), the combination of non-motion and motion data produced the best results. In this case, the flexibility of the spatio-temporal atlas in identifying different motion patterns that are correlated with CRT response was able to complement the non-motion data and improve the results.

In fact, overall, impressive classification results were obtained using non-motion data alone. This is data that is frequently available in the clinical record but is often neglected in the medical image analysis literature. To the best of our knowledge, no work has yet shown how its combination can lead to such impressive results in CRT response prediction. However, this non-motion data comes from a range of sources, and may not always be complete in the clinical record. It is encouraging that our motion descriptors (which are all derived from a single CMR scan) can do as well as, or better than, this diverse range of data.

It is important to remember that CRT treatment planning is not a simple matter of selecting which patients are likely to respond to the treatment. For example, the positions of the pacing leads are known to be a significant factor in the success of CRT treatment, especially in the presence of infarct, i.e. the treatment is not generally successful if a lead is positioned in an infarct (Bilchick et al., 2014). Our work has not focused on this issue, but we believe that our framework could be adapted to identify optimal lead placement, as well as patient selection. In future work, we plan to extend our work to complement the important role that biophysical models have to play in determining optimal lead placement (Sermesant et al., 2012). Furthermore, our framework could be extended to regress more complex functional cardiac variables. As reported in Fornwalt et al. (2009) and Fornwalt (2011), although currently employed as a clinical standard, a binary response classification could be too simplistic as a characterisation of CRT response. In future work, we plan to investigate the extension to a multi-variable regression model, applied to a larger cohort.

Another area for future work is to validate the approach on a larger multi-centre database of CRT patients, to better evaluate the accuracy and robustness of the proposed framework. To facilitate the processing of a large number of CRT datasets, we plan to automate the LV segmentation by learning from previous observations the refinement to the binary masks. A larger patient database would enable other machine learning tasks to be tackled. For example, a multi-class classification could be performed to label patients as either NR, R or SR in a single classification. Regression tasks could also be investigated, such as trying to predict ESV which is used for classifying CRT volumetric response. Furthermore, 3D echocardiography imaging could be employed instead of T-CMR to estimate the motion descriptors, as recently investigated in Puyol-Anton et al. (2016). We would also like to investigate the possibility of including other types of feature into the MKL framework. We have shown how motion and non-motion data can be combined, but the same approach could be employed to incorporate, for example, anatomical features. It would be interesting to discover if a correlation could be found between specific anatomical features and CRT (super-)response, and our framework offers a means of performing such an investigation. The results from such a study could inform further clinical research into the mechanisms underlying CRT response and non-response.

In conclusion, we believe that the work we have presented represents an important contribution to the problem of selecting patients for CRT. In a clinical setting, we would envisage a scenario in which our MKL framework could be used as a screening test for CRT treatment, utilising whatever motion and/or non-motion data were available on a patient-by-patient basis. Furthermore, we believe that our framework offers a way to exploit the important information that motion has to offer, as well as the wealth of data already available in clinical reports. This approach may well have potential application in a much wider range of clinical applications.

Acknowledgements

This work was funded by EPSRC grants EP/K030310/1 and EP/K030523/1. The authors acknowledge financial support from the Department of Health via the National Institute for Health Research (NIHR) comprehensive Biomedical Research Centre award to Guy's & St Thomas' NHS Foundation Trust in partnership with King's College London and King's College Hospital NHS Foundation Trust.

Appendix A. Reorientation of deformation gradient

Let $\mathcal{S}, \mathcal{A} \subseteq \mathbb{R}^3$ denote the LV subject and atlas coordinate system, respectively. The aim is to compute the Green strain $\mathbf{E}_{\mathcal{A}}$ of the LV in the atlas coordinate system as a function of the Green strain $\mathbf{E}_{\mathcal{S}}$ in the subject coordinate system. Let $d\mathbf{X}_{\mathcal{A}} \in \mathbb{R}^3$ be an infinitesimal column vector at the End Diastolic (ED) reference frame in the atlas space and $d\mathbf{x}_{\mathcal{A}} \in \mathbb{R}^3$ be the deformed vector due to the electro-mechanical contraction. The Green strain $\mathbf{E}_{\mathcal{A}} \in \mathbb{R}^{3\times3}$ tensor is then defined as follows

$$\frac{1}{2}\left(l_A^2 - L_A^2\right) = d\mathbf{X}_{\mathcal{A}}^T \mathbf{E}_A d\mathbf{X}_{\mathcal{A}}, \tag{A.1}$$

where

$$l_A^2 = d\mathbf{x}_{\mathcal{A}}^T d\mathbf{x}_{\mathcal{A}}, \quad L_A^2 = d\mathbf{X}_{\mathcal{A}}^T d\mathbf{X}_{\mathcal{A}}. \tag{A.2}$$

Denoting the deformation gradient in the atlas coordinate system by $\mathbf{F}_{\mathcal{A}}$, we have the following

$$d\mathbf{x}_{\mathcal{A}} = \mathbf{F}_{\mathcal{A}} d\mathbf{X}_{\mathcal{A}}. \tag{A.3}$$

By substituting Eq. (A.2) into Eq. (A.1), the Green strain is given by

$$\mathbf{E}_{\mathcal{A}} = \frac{1}{2}\left(\mathbf{F}_{\mathcal{A}}^{T}\mathbf{F}_{\mathcal{A}} - \mathbb{I}\right). \tag{A.4}$$

In similar fashion, the Green strain $\mathbf{E}_{\mathcal{S}}$ is derived from the deformation gradient $\mathbf{F}_{\mathcal{S}}$ in the subject space as

$$\mathbf{E}_{\mathcal{S}} = \frac{1}{2}\left(\mathbf{F}_{\mathcal{S}}^{T}\mathbf{F}_{\mathcal{S}} - \mathbb{I}\right). \tag{A.5}$$

$\mathbf{F}_{\mathcal{S}}$ maps the deformed and reference infinitesimal vectors in the subject coordinate system $d\mathbf{x}_{\mathcal{S}} = \mathbf{F}_{\mathcal{S}} d\mathbf{X}_{\mathcal{S}}$ and is estimated by the motion tracking registration.

We denote by $\mathbf{J}$ the Jacobian of the tranformation mapping the anatomy of subject to the atlas coordinate system at end-diastole, $\mathbf{dX}_A = \mathbf{JdX}$. Therefore, denoting by X and A the coordinates in subject and atlas coordinate system respectively, the deformation gradients can be computed as

$$\frac{\partial \mathbf{u_i}}{\partial X_j} = \frac{\partial \mathbf{u_i}}{\partial A_k}\frac{\partial A_k}{\partial X_j} \rightarrow \nabla_X \mathbf{u} = \nabla_A \mathbf{u}\mathbf{J}. \tag{A.6}$$

If the variation of $\mathbf{J}$ is minimal relative to the variation of $\mathbf{u}$ in A (i.e. $\mathbf{J}$ is locally constant), then

$$\mathbf{F} = \nabla_X \mathbf{u} + \mathbb{I} = \nabla_A(\mathbf{J}^{-1}\mathbf{u}_A)\mathbf{J} + \mathbb{I} \approx \mathbf{J}^{-1}\nabla_A \mathbf{u}_A \mathbf{J} + \mathbb{I} = \mathbf{J}^{-1}\mathbf{F}_A\mathbf{J}. \tag{A.7}$$

By inverting Eq. (A.7), the deformation gradient in the atlas coordinate system is obtained as

$$\mathbf{F}_A = \mathbf{J}\mathbf{F}\mathbf{J}^{-1}. \tag{A.8}$$

References

Abraham, W.T., et al., 2002. Cardiac resynchronization in chronic heart failure. New Engl. J. Med. 346 (24), 1845–1853. doi:10.1056/NEJMoa013168.

António, N., Teixeira, R., Coelho, L.c., Lourenço, C., Monteiro, P., Ventura, M., Cristóvão, J.a., Elvas, L., Gonçalves, L., Providência, L.A., 2009. Identification of 'super-responders' to cardiac resynchronization therapy: the importance of symptom duration and left ventricular geometry. Europace 11 (3), 343–349. doi:10.1093/europace/eup038.

Ardekani, S., Weiss, R.G., Lardo, A.C., George, R.T., Lima, J.A.C., Wu, K.C., Miller, M.I., Winslow, R.L., Younes, L., 2009. Cardiac motion analysis in ischemic and non-ischemic cardiomyopathy using parallel transport. In: Biomedical Imaging: From Nano to Macro, 2009. ISBI '09. IEEE International Symposium on, pp. 899–902. doi:10.1109/ISBI.2009.5193198.

Ashburner, J., 2007. A fast diffeomorphic image registration algorithm. NeuroImage 38 (1), 95–113. http://dx.doi.org/10.1016/j.neuroimage.2007.07.007.

Bai, W., Shi, W., de Marvao, A., Dawes, T.J.W., Regan, D.P.O., Cook, S.A., Rueckert, D., 2015. A bi-ventricular cardiac atlas built from 1000+ high resolution MR images of healthy subjects and an analysis of shape and motion. Med. Image Anal. 26 (1), 133–145. http://dx.doi.org/10.1016/j.media.2015.08.009.

Bilchick, K.C., Kuruvilla, S., Hamirani, Y.S., Ramachandran, R., Clarke, S.A., Parker, K.M., Stukenborg, G.J., Mason, P., Ferguson, J.D., Moorman, J.R., Malhotra, R., Mangrum, J.M., Darby, A.E., DiMarco, J., Holmes, J.W., Salerno, M., Kramer, C.M., Epstein, F.H., 2014. Impact of mechanical activation, scar, and electrical timing on cardiac resynchronization therapy response and clinical outcomes. J. Am. College Cardiol. 63 (16), 1657–1666. http://dx.doi.org/10.1016/j.jacc.2014.02.533.

Bleeker, G.B., Bax, J.J., Fung, J.W.-H., van der Wall, E.E., Zhang, Q., Schalij, M.J., Chan, J.Y.-S., Yu, C.-M., 2006. Clinical versus echocardiographic parameters to assess response to cardiac resynchronization therapy. Am. J. Cardiol. 97 (2), 260–263. http://dx.doi.org/10.1016/j.amjcard.2005.08.030.

Bonet, J., Wood, R.D., 2008. Nonlinear Continuum Mechanics for Finite Element Analysis, 2nd ed. Cambridge University Press. Cambridge Books Online.

Chandrashekara, R., Mohiaddin, R.H., Rueckert, D., 2004. Analysis of 3-D myocardial motion in tagged MR images using nonrigid image registration. IEEE Trans. Med. Imag. 23 (10), 1245–1250. doi:10.1109/TMI.2004.834607.

Chandrashekara, R., Rao, A., Sanchez-Ortiz, G.I., Mohiaddin, R.H., Rueckert, D., 2003. Construction of a statistical model for cardiac motion analysis using nonrigid image registration. In: Taylor, C., Noble, J. (Eds.), Information Processing in Medical Imaging. In: Lecture Notes in Computer Science, vol. 2732. Springer Berlin Heidelberg, pp. 599–610. doi:10.1007/978-3-540-45087-0_50.

Chung, E.S., Leon, A.R., Tavazzi, L., Sun, J.-P., Nihoyannopoulos, P., Merlino, J., Abraham, W.T., Ghio, S., Leclercq, C., Bax, J.J., Yu, C.-M., Gorcsan, J., St John Sutton, M., De Sutter, J., Murillo, J., 2008. Results of the predictors of response to CRT (PROSPECT) trial. Circulation 117 (20), 2608–2616. doi:10.1161/CIRCULATIONAHA.107.743120.

Costa, J.A., Hero III, A.O., 2005. Classification constrained dimensionality reduction. In: 2005 IEEE International Conference on Acoustics, Speech, and Signal Processing, ICASSP '05, Philadelphia, Pennsylvania, USA, March 18–23, 2005, pp. 1077–1080. doi:10.1109/ICASSP.2005.1416494.

Daubert, J.-C., Saxon, L., Adamson, P.B., Auricchio, A., Berger, R.D., Beshai, J.F., Breithard, O., Brignole, M., Cleland, J., DeLurgio, D.B., Dickstein, K., Exner, D.V., Gold, M., Grimm, R.A., Hayes, D.L., Israel, C., Leclercq, C., Linde, C., Lindenfeld, J., Merkely, B., Mont, L., Murgatroyd, F., Prinzen, F., Saba, S.F., Shinbane, J.S., Singh, J., Tang, A.S., Vardas, P.E., Wilkoff, B.L., Zamorano, J.L., Anand, I., Blomström-Lundqvist, C., Boehmer, J.P., Calkins, H., Cazeau, S., Delgado, V., Estes, N.A.M., Haines, D., Kusumoto, F., Leyva, P., Ruschitzka, F., Stevenson, L.W., Torp-Pedersen, C.T., 2012. 2012 EHRA/HRS expert consensus statement on cardiac resynchronization therapy in heart failure: implant and follow-up recommendations and management. Europace 14 (9), 1236–1286. doi:10.1093/europace/eus222.

De Craene, M., Duchateau, N., Tobon-Gomez, C., Ghafaryasl, B., Piella, G., Rhode, K.S., Frange, A.F., 2012. SPM to the heart: mapping of 4d continuous velocities for motion abnormality quantification. In: Biomedical Imaging (ISBI), 2012 9th IEEE International Symposium on, pp. 454–457. doi:10.1109/ISBI.2012.6235582.

Duchateau, N., De Craene, M., Pennec, X., Merino, B., Sitges, M., Bijnens, B., 2012. Which reorientation framework for the atlas-based comparison of motion from cardiac image sequences? In: Durrleman, S., Fletcher, T., Gerig, G., Niethammer, M. (Eds.), Spatio-temporal Image Analysis for Longitudinal and Time-Series Image Data. Lecture Notes in Computer Science, vol. 7570. Springer Berlin Heidelberg, pp. 25–37. doi:10.1007/978-3-642-33555-6_3.

Duchateau, N., De Craene, M., Piella, G., Frangi, A.F., 2012. Constrained manifold learning for the characterization of pathological deviations from normality. Med. Image Anal. 16 (8), 1532–1549. http://dx.doi.org/10.1016/j.media.2012.07.003.

Duchateau, N., De Craene, M., Piella, G., Hoogendoorn, C., Silva, E., Doltra, A., Mont, L., Castel, M., Brugada, J., Sitges, M., Frangi, A.F., 2010. Atlas-based quantification of myocardial motion abnormalities: added-value for the understanding of CRT outcome? In: Camara, O., Pop, M., Rhode, K., Sermesant, M., Smith, N., Young, A. (Eds.), Statistical Atlases and Computational Models of the Heart. Lecture Notes in Computer Science, vol. 6364. Springer Berlin Heidelberg, pp. 65–74. doi:10.1007/978-3-642-15835-3_7.

Duchateau, N., De Craene, M., Piella, G., Silva, E., Doltra, A., Sitges, M., Bijnens, B.H., Frangi, A.F., 2011. A spatiotemporal statistical atlas of motion for the quantification of abnormal myocardial tissue velocities. Med. Image Anal. 15 (3), 316–328. http://dx.doi.org/10.1016/j.media.2010.12.006.

Enright, P.L., 2003. The six-minute walk test. Respir. Care 48 (8), 783–785.

Filipovych, R., Resnick, S., Davatzikos, C., 2011. Multi-kernel classification for integration of clinical and imaging data: application to prediction of cognitive decline in older adults. In: Suzuki, K., Wang, F., Shen, D., Yan, P. (Eds.), Machine Learning in Medical Imaging. Lecture Notes in Computer Science, vol. 7009. Springer Berlin Heidelberg, pp. 26–34. doi:10.1007/978-3-642-24319-6_4.

Fornwalt, B.K., 2011. The dyssynchrony in predicting response to cardiac resynchronization therapy: a call for change. J. Am. Soc. Echocardiogr. 24, 180–184.

Fornwalt, B.K., Delfino, J.G., Sprague, W.W., Oshinski, J.N., 2009. Its time for a paradigm shift in the quantitative evaluation of left ventricular dyssynchrony. J. Am. Soc. Echocardiogr. 22, 672–676.

Garcia-Barnes, J., Gil, D., Badiella, L., Hernandez-Sabate, A., Carreras, F., Pujades, S., Marti, E., 2010. A normalized framework for the design of feature spaces assessing the left ventricular function. Med. Imaging IEEE Trans. 29 (3), 733–745. doi:10.1109/TMI.2009.2034653.

Hegde, C., Wakin, M., Baraniuk, R., 2008. Random projections for manifold learning. In: Platt, J., Koller, D., Singer, Y., Roweis, S. (Eds.), Advances in Neural Information Processing Systems 20. Curran Associates, Inc., pp. 641–648.

Hinrichs, C., Singh, V., Xu, G., Johnson, S., 2009. MKL for robust multi-modality AD classification. In: Yang, G.-Z., Hawkes, D., Rueckert, D., Noble, A., Taylor, C. (Eds.), Medical Image Computing and Computer-Assisted Intervention MICCAI 2009. Lecture Notes in Computer Science, vol. 5762. Springer Berlin Heidelberg, pp. 786–794. doi:10.1007/978-3-642-04271-3_95.

Hoogendoorn, C., Duchateau, N., Sanchez-Quintana, D., Whitmarsh, T., Sukno, F.M., De Craene, M., Lekadir, K., Frangi, A.F., 2013. A high-resolution atlas and statistical model of the human heart from multislice CT. Med. Imaging IEEE Trans. 32 (1), 28–44. doi:10.1109/TMI.2012.2230015.

Jackson, T., Sohal, M., Chen, Z., Child, N., Sammut, E., Behar, J., Claridge, S., Carr-White, G., Razavi, R., Rinaldi, C.A., 2014. A U-shaped type II contraction pattern in patients with strict left bundle branch block predicts super-response to cardiac resynchronization therapy. Heart Rhythm 11 (10), 1790–1797, Focus Issue: Sudden Death. http://dx.doi.org/10.1016/j.hrthm.2014.06.005.

Johnson, W.B., Lindenstrauss, J., 1984. Extensions of Lipschitz mappings into Hilbert spaces. Contemp. Math. 26, 189–206.

Kirk, J.A., Kass, D.A., 2013. Electromechanical dyssynchrony and resynchronization of the failing heart. Circ. Res. 113 (6), 765–776. doi:10.1161/CIRCRESAHA.113.300270.

Lin, Y.Y., Liu, T.L., Fuh, C.S., 2011. Multiple kernel learning for dimensionality reduction. IEEE Trans. Pattern Anal. Mach. Intell. 33 (6), 1147–1160. doi:10.1109/TPAMI.2010.183.

Lorenzi, M., Ayache, N., Pennec, X., 2011. Schild's ladder for the parallel transport of deformations in time series of images. In: Szkely, G., Hahn, H. (Eds.), Information Processing in Medical Imaging. Lecture Notes in Computer Science, vol. 6801. Springer Berlin Heidelberg, pp. 463–474. doi:10.1007/978-3-642-22092-0_38.

Lu, Y., Radau, P., Connelly, K., Dick, A., Wright, G., 2009. Pattern recognition of abnormal left ventricle wall motion in cardiac MR. In: Yang, G.-Z., Hawkes, D., Rueckert, D., Noble, A., Taylor, C. (Eds.), Medical Image Computing and Computer-Assisted Intervention MICCAI 2009. Lecture Notes in Computer Science, vol. 5762. Springer Berlin Heidelberg, pp. 750–758. doi:10.1007/978-3-642-04271-3_91.

Maret, E., Todt, T., Brudin, L., Nylander, E., Swahn, E., Ohlsson, J., Engvall, J., 2009. Functional measurements based on feature tracking of cine magnetic resonance images identify left ventricular segments with myocardial scar. Cardiovasc. Ultrasound 7 (1). doi:10.1186/1476-7120-7-53.

McLeod, K., Sermesant, M., Beerbaum, P., Pennec, X., 2015. Descriptive and intuitive population-based cardiac motion analysis via sparsity constrained tensor decomposition. Medical Image Computing and Computer Assisted Intervention (MICCAI 2015). Munich, Germany.

McLeod, K., Sermesant, M., Beerbaum, P., Pennec, X., 2015. Spatio-temporal tensor decomposition of a polyaffine motion model for a better analysis of pathological left ventricular dynamics. Med. Imaging IEEE Trans. 34 (7), 1562–1575.

Medrano-Gracia, P., Cowan, B., Bluemke, D., Finn, J., Kadish, A., Lee, D., Lima, J.C., Suinesiaputra, A., Young, A., 2014. Continuous spatio-temporal atlases of the asymptomatic and infarcted hearts. In: Camara, O., Mansi, T., Pop, M., Rhode, K., Sermesant, M., Young, A. (Eds.), Statistical Atlases and Computational Models of the Heart. Imaging and Modelling Challenges. Lecture Notes in Computer Science, vol. 8330. Springer Berlin Heidelberg, pp. 143–151. doi:10.1007/978-3-642-54268-8_17.

Medrano-Gracia, P., Suinesiaputra, A., Cowan, B., Bluemke, D., Frangi, A., Lee, D., Lima, J., Young, A., 2013. An atlas for cardiac MRI regional wall motion and infarct scoring. In: Camara, O., Mansi, T., Pop, M., Rhode, K., Sermesant, M., Young, A. (Eds.), Statistical Atlases and Computational Models of the Heart. Imaging and Modelling Challenges. Lecture Notes in Computer Science, vol. 7746. Springer Berlin Heidelberg, pp. 188–197. doi:10.1007/978-3-642-36961-2_22.

Owen, J.S., Khatib, S., Morin, D.P., 2009. Cardiac resynchronization therapy. Ochsner J. 9 (4), 248–256.

Parsai, C., Bijnens, B., Sutherland, G.R., Baltabaeva, A., Claus, P., Marciniak, M., Paul, V., Scheffer, M., Donal, E., Derumeaux, G., Anderson, L., 2009. Toward understanding response to cardiac resynchronization therapy: left ventricular dyssynchrony is only one of multiple mechanisms. Eur. Heart J. 30 (8), 940–949. doi:10.1093/eurheartj/ehn481.

Peressutti, D., Bai, W., Jackson, T., Sohal, M., Rinaldi, A., Rueckert, D., King, A., 2015. Prospective identification of CRT super responders using a motion atlas and random projection ensemble learning. In: Navab, N., Hornegger, J., Wells, W., Frangi, A. (Eds.), Medical Image Computing and Computer-Assisted Intervention MICCAI 2015. Lecture Notes in Computer Science, vol. 9351. Springer International Publishing, pp. 493–500. doi:10.1007/978-3-319-24574-4_59.

Perperidis, D., Mohiaddin, R., Rueckert, D., 2005. Construction of a 4d statistical atlas of the cardiac anatomy and its use in classification. In: Duncan, J., Gerig, G. (Eds.), Medical Image Computing and Computer-Assisted Intervention MICCAI 2005. Lecture Notes in Computer Science, vol. 3750. Springer Berlin Heidelberg, pp. 402–410. doi:10.1007/11566489_50.

Puyol-Anton, E., Peressutti, D., Aljabar, P., De Craene, M., Piro, P., King, A., 2016. Towards a multi-modal cardiac motion atlas for biomarker extraction. In: Proceedings of IEEE International Symposium on Biomedical Imaging, 2016.

Qiu, A., Albert, M., Younes, L., Miller, M.I., 2009. Time sequence diffeomorphic metric mapping and parallel transport track time-dependent shape changes. NeuroImage 45 (1, Supplement 1), S51–S60, Mathematics in Brain Imaging. http://dx.doi.org/10.1016/j.neuroimage.2008.10.039.

Rakotomamonjy, A., Bach, F., Canu, S., Grandvalet, Y., 2008. SimpleMKL. Journal of Machine Learning Research 9, 2491–2521.

Rao, A., Chandrashekara, R., Sanchez-Ortiz, G.I., Mohiaddin, R., Aljabar, P., Hajnal, J.V., Puri, B.K., Rueckert, D., 2004. Spatial transformation of motion and deformation fields using nonrigid registration. IEEE Trans. Med. Imaging 23 (9), 1065–1076. doi:10.1109/TMI.2004.828681.

Rao, A., Sanchez-Ortiz, G.I., Chandrashekara, R., Lorenzo-ValdÈ¨s, M., Mohiaddin, R., Rueckert, D., 2002. Comparison of cardiac motion across subjects using non-rigid registration. In: Medical Image Computing and Computer-Assisted Intervention - MICCAI 2002, vol. 2488. Springer Berlin Heidelberg, pp. 722–729. doi:10.1007/3-540-45786-0_89.

Rougon, N.F., Petitjean, C., Preteux, F.J., 2004. Building and using a statistical 3d motion atlas for analyzing myocardial contraction in MRI. In: SPIE Medical Imaging, Vol. 5370, pp. 253–264. doi:10.1117/12.535609.

Rueckert, D., Sonoda, L.I., Hayes, C., Hill, D.L.G., Leach, M.O., Hawkes, D.J., 1999. Non-rigid registration using free-form deformations: application to breast MR images. IEEE Trans. Med. Imaging 18 (8), 712–721. doi:10.1109/42.796284.

Sanchez-Martinez, S., Duchateau, N., Bijnens, B., Erdei, T., Fraser, A., Piella, G., 2015. Characterization of myocardial velocities by multiple kernel learning: application to heart failure with preserved ejection fraction. In: van Assen, H., Bovendeerd, P., Delhaas, T. (Eds.), Functional Imaging and Modeling of the Heart. Lecture Notes in Computer Science, vol. 9126. Springer International Publishing, pp. 65–73. doi:10.1007/978-3-319-20309-6_8.

Santaularia-Tomas, M., Abraham, T.P., 2009. Criteria predicting response to CRT: is more better? Eur. Heart J. 30 (23), 2835–2837. doi:10.1093/eurheartj/ehp378.

Sermesant, M., Chabiniok, R., Chinchapatnam, P., Mansi, T., Billet, F., Moireau, P., Peyrat, J.M., Wong, K., Relan, J., Rhode, K., Ginks, M., Lambiase, P., Delingette, H., Sorine, M., Rinaldi, C.A., Chapelle, D., Razavi, R., Ayache, N.., 2012. Patient-specific electromechanical models of the heart for the prediction of pacing acute effects in CRT: a preliminary clinical validation. Med. Image Anal. 16 (1), 201–215.

Shi, W., Zhuang, X., Wang, H., Duckett, S., Luong, D.V.N., Tobon-Gomez, C., Tung, K.P., Edwards, P.J., Rhode, K.S., Razavi, R.S., Ourselin, S., Rueckert, D., 2012. A comprehensive cardiac motion estimation framework using both untagged and 3-D tagged MR images based on nonrigid registration. Med. Imaging IEEE Trans. 31 (6), 1263–1275. doi:10.1109/TMI.2012.2188104.

Sohal, M., Duckett, S., Zhuang, X., Shi, W., Ginks, M., Shetty, A., Sammut, E., Kozerke, S., Niederer, S., Smith, N., Ourselin, S., Rinaldi, C., Rueckert, D., Carr-White, G., Razavi, R., 2014. A prospective evaluation of cardiovascular magnetic resonance measures of dyssynchrony in the prediction of response to cardiac resynchronization therapy. J. Cardiovasc. Magn. Reson. 16 (1), 58. doi:10.1186/s12968-014-0058-0.

Sohal, M., Shetty, A., Duckett, S., Chen, Z., Sammut, E., Amraoui, S., Carr-White, G., Razavi, R., Rinaldi, C.A., 2013. Noninvasive assessment of LV contraction patterns using CMR to identify responders to CRT. JACC 6 (8), 864–873. http://dx.doi.org/10.1016/j.jcmg.2012.11.019.

Suinesiaputra, A., Frangi, A.F., Kaandorp, T., Lamb, H.J., Bax, J.J., Reiber, J., Lelieveldt, B.P.F., 2009. Automated detection of regional wall motion abnormalities based on a statistical model applied to multislice short-axis cardiac MR images. Med. Imaging IEEE Trans. 28 (4), 595–607. doi:10.1109/TMI.2008.2008966.

Tian, Y., Zhang, P., Li, X., Gao, Y., Zhu, T., Wang, L., Li, D., Wang, J., Yuan, C., Guo, J., 2013. True complete left bundle branch block morphology strongly predicts good response to cardiac resynchronization therapy. Europace 15 (10), 1499–1506. doi:10.1093/europace/eut049.

Tobon-Gomez, C., De Craene, M., McLeod, K., Tautz, L., Shi, W., Hennemuth, A., Prakosa, A., Wang, H., Carr-White, G., Kapetanakis, S., Lutz, A., Rasche, V., Schaeffter, T., Butakoff, C., Friman, O., Mansi, T., Sermesant, M., Zhuang, X., Ourselin, S., Peitgen, H.-O., Pennec, X., Razavi, R., Rueckert, D., Frangi, A.F., Rhode, K.S., 2013. Benchmarking framework for myocardial tracking and deformation algorithms: an open access database. Medical image analysis 17 (6), 632–648. http://dx.doi.org/10.1016/j.media.2013.03.008.

White, H.D., Norris, R.M., Brown, M.A., Brandt, P.W., Whitlock, R.M., Wild, C.J., 1987. Left ventricular end-systolic volume as the major determinant of survival after recovery from myocardial infarction.. Circulation 76 (1), 44–51. doi:10.1161/01.CIR.76.1.44.

Wolz, R., Aljabar, P., Hajnal, J.V., Lotjonen, J., Rueckert, D., 2012. Nonlinear dimensionality reduction combining MR imaging with non-imaging information. Med. Image Anal. 16 (4), 819–830. http://dx.doi.org/10.1016/j.media.2011.12.003.

Yan, S., Xu, D., Zhang, B., Zhang, H.j., Yang, Q., Lin, S., 2007. Graph embedding and extensions: a general framework for dimensionality reduction. IEEE Trans. Pattern Anal. Mach. Intell. 29 (1), 40–51. doi:10.1109/TPAMI.2007.250598.

Ypenburg, C., van Bommel, R.J., Borleffs, C.J.W., Bleeker, G.B., Boersma, E., Schalij, M.J., Bax, J.J., 2009. Long-term prognosis after cardiac resynchronization therapy is related to the extent of left ventricular reverse remodeling at midterm follow-up. J. Am. College Cardiol. 53 (6), 483–490. doi:10.1016/j.jacc.2008.10.032.